JGR Solid Earth

Correspondence to:
S. Jin,
sgjin@shao.ac.cn;
sg.jin@yahoo.com

Characterization of Irreversible Land Subsidence in the Yazd-Ardakan Plain, Iran From 2003 to 2020 InSAR Time Series

Sayyed Mohammad Javad Mirzadeh[1,2] , Shuanggen Jin[1,3] , Esmaeel Parizi[4] , Estelle Chaussard[5] , Roland Bürgmann[6] , Jose Manuel Delgado Blasco[7] , Meisam Amani[8] , Han Bao[9] , and Seyyed Hossein Mirzadeh[10]

[1]Shanghai Astronomical Observatory, Chinese Academy of Sciences, Shanghai, China, [2]School of Astronomy and Space Science, University of Chinese Academy of Sciences, Beijing, China, [3]School of Remote Sensing and Geomatics Engineering, Nanjing University of Information Science and Technology, Nanjing, China, [4]Physical Geography Department, University of Tehran, Tehran, Iran, [5]Independent Researcher, [6]Department of Earth and Planetary Science, University of California Berkeley, Berkeley, CA, USA, [7]Grupo de Investigación Microgeodesia Jaén (PAIDI RNM-282), Universidad de Jaén, Jaén, Spain, [8]Wood Environment & Infrastructure Solutions, Ottawa, ON, Canada, [9]Earth, Planetary, and Space Sciences, University of California, Los Angeles, CA, USA, [10]Faculty of Architecture and Urban Planning, University of Art, Tehran, Iran

Abstract Groundwater extraction rates exceeding recharge are occurring throughout Iran to sustain industrial and agricultural activities, resulting in land deformation in many areas, particularly in the Yazd-Ardakan Plain (YAP) in central Iran's dry and desert regions. In this study, Interferometric Synthetic Aperture Radar (InSAR) time series analysis and statistical models are applied to characterize the controls on land subsidence in the YAP from 2003 to 2020. Our results reveal the existence of a northwest-southeast elongated area of 234.45 km^2 experiencing subsidence at rates up to 15 cm/yr. In the YAP, the international Airport, railway, transit road, and several industrial and historical sites are threatened by the differential subsidence. Well data confirm that groundwater levels have decreased by 18 meters between 1974 and 2018, driving the compaction of sediments within the underlying aquifer system. Our statistical analysis shows that the thickness of a shallow, clay-rich aquitard layer controls the extent of the observed subsidence and the Independent Component Analysis of the InSAR time series shows that inelastic compaction is dominated. This work reveals that current groundwater extraction practices in central Iran are not sustainable and result in permanent subsidence, ground fractures with impact on infrastructures, and a permanent decrease in water storage capacity.

Plain Language Summary As the world's population grows, the pressure on finite water resources intensifies, especially in desert areas around the world. Groundwater extraction is often accompanied by many ancillary problems such as land subsidence. In this work, we show that the measurements of such land subsidence from satellites can be used to inform many aspects of water sustainability management plans, which are necessary to develop and implement in the Yazd-Ardakan Plain (YAP) of Central Iran. Between 2003 and 2020, our ground deformation data in this area highlight (a) subsidence up to 15 cm/yr, (b) damage to several strategic infrastructures, (c) a significant yearly groundwater storage loss, and (d) the controls on the land subsidence. This work reveals that permanent, irrecoverable compaction dominates, mostly controlled by sediments in the subsurface, and reveals that the current groundwater extraction practices in central Iran are not sustainable. This work is complementary to the previous studies, providing essential and important data to investigate the possibility of the collapse of the surface layer and the distribution of fractures in the YAP.

1. Introduction

Deserts and semi-deserts currently comprise more than one-third of the global land surface (Laity, 2009). In these areas, recent climatic changes (i.e., increasing temperature and decreasing precipitation) occur at a faster rate than in other environments (Porter et al., 2014). These changes result in the loss of valuable topsoil by wind erosion, soil salinization, loss of sparse vegetation, and dropping groundwater levels (Laity, 2009). In addition, the population growth and industrial and urban developments in desert areas have

resulted in increasing exploitation of underground water resources (Avtar et al., 2019), which leads to land subsidence. Land subsidence is well-known in desert and semi-desert areas such as the Las Vegas Valley, Nevada, USA (Amelung et al., 1999), the Avra Valley, Arizona, USA (Hanson et al., 1990), the Mojave Desert, California, USA (Galloway et al., 1998), Mexico's San Luis Potosı́ state and Mexico City (Chaussard et al., 2021; Julio-Miranda et al., 2012), South Kordofan state, Sudan (Gido et al., 2020), Saudi Arabia (Amin & Bankher, 1997), and Kerman and Yazd regions of Iran (Motagh et al., 2008). Several outcomes are related to land subsidence such as accelerated erosion along earth fissures, drainage systems, degradation and contamination of groundwater, damage to infrastructure and structures, and socio-economic impacts (Abidin et al., 2001; Chaussard et al., 2021; Conway, 2016). Therefore, it is important to monitor and investigate both the temporal variability and spatial extent of land subsidence to establish a continuous monitoring system and to assist in the development of a sustainable water management program (Baum et al., 2008; Emil et al., 2018).

Although ground-based geodetic surveys such as precise differential leveling and Global Navigation Satellite System (GNSS) (Jin & Park, 2006; Jin & Su, 2020) are accurate techniques for monitoring land subsidence, these approaches are costly and also spatially limited (Galloway & Burbey, 2011). Remote sensing techniques can be used to map and evaluate the sub-centimeter ground displacement with a high spatial resolution (tens to hundreds meters) over large areas (tens to thousands of square kilometers), and are thus well suited for monitoring land subsidence (e.g., Chaussard et al. (2013); Chaussard, Wdowinski, et al. (2014)). Interferometric synthetic aperture radar (InSAR) enables quantifying surface topography and its changes over large regions (Bürgmann et al., 2000). InSAR uses several Synthetic Aperture Radar (SAR) images of the same area acquired at different times by a single antenna or at the same time by two antennas separated in an along-track direction. InSAR has offered insights into the hydrogeological and geological processes in deforming aquifers (Bell et al., 2008; Bozzano et al., 2015; Chaussard et al., 2017; Hoffmann et al., 2001; Hu et al., 2018; Ojha et al., 2018; Schmidt & Bürgmann, 2003; Tenzer et al., 2015).

In Iran, intense irrigation of agricultural needs and rapid urban development are the main sources of groundwater over-drafting and cause depletion of water reservoirs (e.g., Anderssohn et al. (2008)). Throughout the country, the volume of annual groundwater extraction increased from 20 billion m^3 in 1960 to more than 53 billion m^3 in 2003 (World Bank, 2005). Land subsidence is documented in more than 300 plains or sedimentary basins of Iran (Amighpey & Arabi, 2016; Anderssohn et al., 2008; Babaee et al., 2020). Motagh et al. (2017) explored land subsidence in the Rafsanjan plain with InSAR time series analysis of Envisat, ALOS-1, and Sentinel-1 datasets between 2004 and 2016, revealing subsidence exceeding 30 cm/yr. Haghighi and Motagh (2019) reported three discrete subsidence zones with rates up to 25 cm/yr in the capital of Iran, Tehran, using 2003–2017 time series analysis of the Envisat, TerraSAR-X, ALOS, and Sentinel-1 data, and showed that inelastic (permanent) compaction was dominated in this aquifer.

The Yazd-Ardakan Plain (YAP) is one of the main strategic regions in Iran in terms of aggregation of infrastructures, industrial sites, and transportation corridors (Figure 1, Table S2) (Esfanjary, 2018). Increasing demand for water resources in recent decades, due to population growth and industrial and agricultural developments, has led to groundwater depletion and subsidence (Amighpey & Arabi, 2016). In this study, we quantify the spatiotemporal evolution of land subsidence in the YAP using InSAR time series analysis to resolve the underlying controls on subsidence rates and spatial extent. The Small BAseline Subset (SBAS) time series technique (Berardino et al., 2002; Hooper, 2008) was implemented using both the Envisat and Sentinel-1 datasets to derive time-dependent subsidence between 2003 and 2020. InSAR time series results were then analyzed with an Independent Component Analysis (ICA) to separate contributions from elastic (i.e., reversible) and inelastic (i.e., irreversible) deformation (Chaussard & Farr, 2019). Finally, hydrogeological and geological parameters were combined using statistical and artificial intelligence methods to quantify the dominant control(s) on the observed deformation in the YAP aquifer.
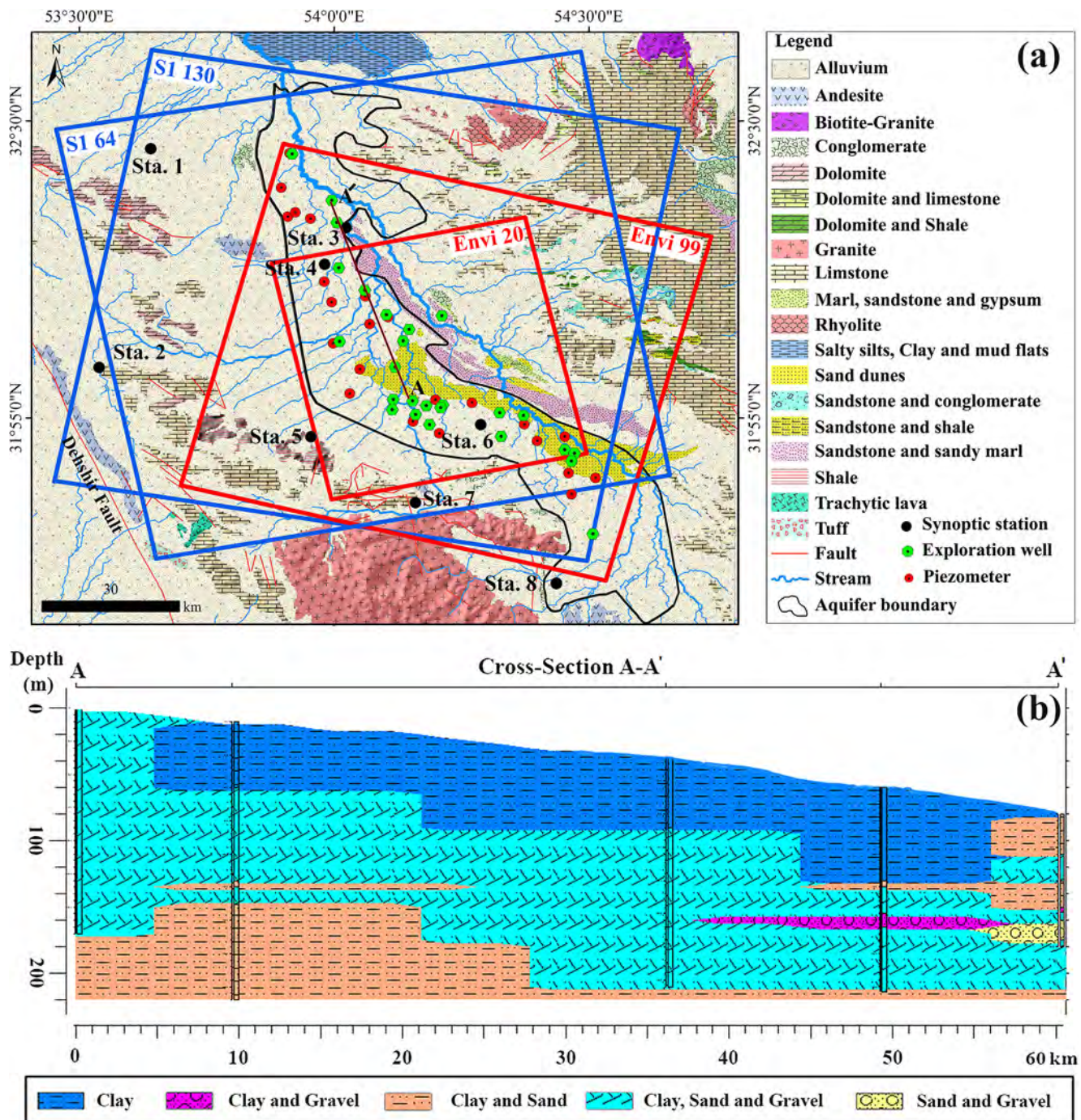
2. Yazd-Ardakan Plain

The YAP is located between 53.65 and 54.77 E longitude and 31.55 and 32.50 N latitude in the central part of the province of Yazd (Figure 1). The elevation in this region rises from 997 to 2677 m above sea level from the north towards the south.
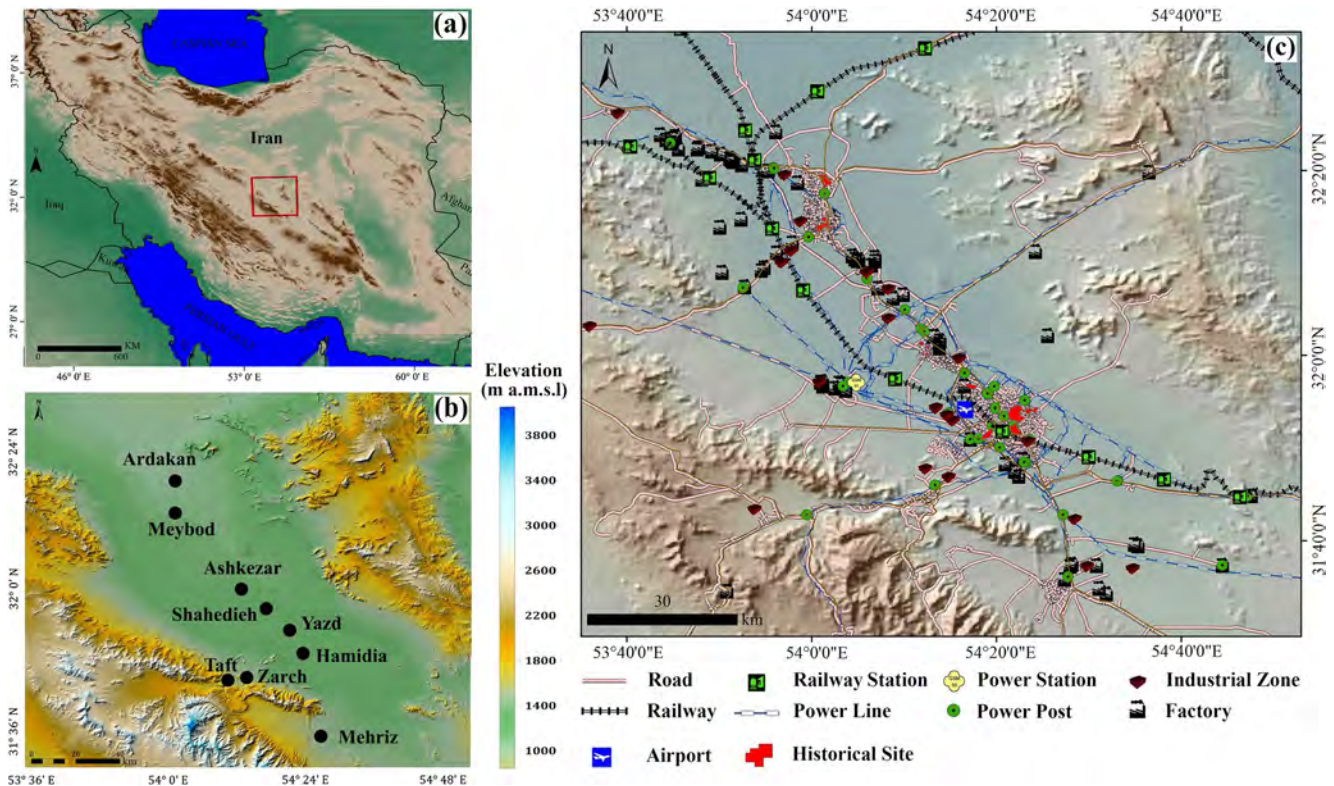
Figure 1. (a) Location of Yazd-Ardakan Plain (YAP) in Iran, indicated with a red rectangle. (b) Topography of the YAP with black dots showing the cities of Ardakan, Meybod, Ashkezar, Shahedieh, Yazd, Hamidia, Zarch, Taft, and Mehriz. (c) Main infrastructures, industrial and historical sites located in the YAP (see Table S2).

The YAP is a dry desert with average annual evaporation of ∼2900 mm and average annual rainfall of ∼130 mm (TAMAB, 2004) based on recorded data during 1969–2011. Within the YAP, there is no year-round surface water and, accordingly, cities have relied on groundwater delivered through qanats (a system of connected underground wells). The YAP aquifer covers an area of 2618.57 km² (Figure 2a). This confined aquifer is topped by a tens-of-meters thick clay-rich aquitard layer in the central part of the valley (light-blue in Figure 2b). Groundwater levels are measured monthly by the Iran Water Resources Management (TAMAB, 2004) using 81 piezometers, which reveal maximum and minimum depths to water levels of 164.6 and 8.12 m, respectively (Regional Water Company of Yazd, 2014). Table S1 provides the estimated discharge and recharge components of the long-term groundwater balance in the YAP over 30 years (1981–2011), which shows that the primary source of aquifer discharge is withdrawal through pumping wells, qanats, and springs at 323.14 million m³ per year (Figure S1). A key contribution to aquifer recharge comes from the return of wastewater from the agricultural sector at 84.14 million m³ per year, while recharge by precipitation amounts to only 11.53 million m³ per year and loss by evaporation from groundwater was estimated to be insignificant (Regional Water Company of Yazd, 2014). A large net storage loss of ∼65.93 million m³ per year (the difference between discharge and recharge components in Table S1) has led the Water Resource Company of Ministry of Energy to label the YAP as a "forbidden" aquifer, a term used to refer to the most imperiled aquifers in Iran (Regional Water Company of Yazd, 2014).

Figure 2a shows the Jurassic to Quaternary lithologies observed in the YAP. Quaternary sediments cover the largest part of the YAP with 74.6% of this area, consisting of sand dunes, alluvium, and sabkha (salty silts, clays, and salt flats). The Dehshir fault, a 400 km-long NNW-trend strike-slip fault (Walker & Jackson, 2004) with an estimated right-lateral slip rate of 2 mm per year (Walker et al., 2009), is bounding the YAP to the southwest (red line in Figure 2a).

Figure 2. (a) Geological map of the Yazd-Ardakan Plain (YAP) modified from the Geological Survey of Iran (1997). Black lines represent the confined aquifer boundary. Brown line shows the location of cross-section (A-A'). Red and green dots show the locations of piezometers and exploration wells, respectively. Black dots, labeled by Sta.1 to Sta. 8, show the locations of synoptic stations, Aqda, NasrAbad, Ardakan, Meybod, Sadoogh, Yazd, Taft, and Mehriz. Outline of frames from Sentinel-1 and Envisat tracks in the ascending and descending orbit directions are shown with the blue and red rectangles, respectively. (b) Geologic cross-section of the YAP aquifer along A-A' relying on data from the exploration wells shown in (a). They show that the geological materials of the aquifer are mostly unconsolidated sediments (clay and sand: orange; sand and gravel: yellow; clay, sand, and gravel mix: cyan; and gravel and clay: purple), and their thickness decreases from the south (left) to the north (right). The topmost clay unit (blue) corresponds to the confining aquitard layer.

3. Data and Methods

3.1. Data

3.1.1. SAR Satellite Data

248 Sentinel-1 images acquired in Interferometric Wide-swath (IW) mode from the Alaska Satellite Facility (ASF), and 40 Envisat ASAR images in StripMap (SM) mode from the European Space Agency (ESA) are used. Sentinel-1 images were acquired from October 2014 to March 2020 from both descending and ascending orbits (Figure 2a) with a resolution of 5 × 20 m (Range × Azimuth) (Table S3). The Envisat ASAR images were acquired from March 2003 to October 2010 and from September 2004 to July 2010 from the descending and ascending orbits, respectively (Figure 2a), with a resolution of 8 × 4 m (Range × Azimuth) (Table S4).

3.1.2. Hydrological Data

Monthly data from 23 piezometers are used to assess groundwater level (GWL) variations between 2004 and 2018 (Figure 2a). We use an Inverse Distance Weighted (IDW) (ESRI, 2012; Gong et al., 2014) approach to produce a map of annual GWL changes (Figure S2c). The Kernel Density method (Trabelsi et al., 2016) was used to map the density of pumping wells (Figure S2b) and the annual pumping volume (Figure S2d) by interpolation of 1194 pumping wells data (Figure S2f). Aquifer transmissivity is one of the most important properties affecting yields of a pumping well. It is equal to the product of the aquifer thickness (m) and hydraulic conductivity (K) and describes an aquifer's capacity to transmit water (Cheremisinoff, 1998; Sterrett, 2007). A transmissivity map (Figure S2e) was generated by interpolating transmissivity point data from pumping tests (Parizi et al., 2019; Regional Water Company of Yazd, 2014).

3.1.3. Geological Data

Stratigraphic data within the YAP (Figure 2a) are derived from the geological map at a scale of 1:100000 provided and distributed by the Geological Survey and Mineral Explorations of Iran (GSI) (Geological Survey of Iran, 1997). The logs of 26 exploration wells (Figure 2a; TAMAB (2004)) were utilized to derive the spatial distribution and thickness of clay sediments (Figure S2a) with an IDW approach (ESRI, 2012; Gong et al., 2014).

3.1.4. Weather Data

Time-series of Land Surface Temperature (LST) were generated using the MODIS/Terra product MOD11_L2 swath that provides daily LST and emissivity values with a resolution of 1 km in a 1200 km × 1200 km grid (Figures S3a and S3b). Time series of precipitation were generated using the daily precipitation data of eight stations (see their locations in Figure 2a) distributed in the YAP (Iran Meteorological Organization, 2018) (Figure S3c). The Temperature-Vegetation-soil Moisture Dryness Index (TVMDI) was computed using (a) LST data, (b) Soil Moisture (SM) data, and (c) Perpendicular Vegetation Index (PVI) in the form of

$$\text{TVMDI} = \sqrt{\text{LST}^2 + \text{SM}^2 + \left(\sqrt{3}/3 - \text{PVI}\right)^2},$$ used to assess the pattern of dryness over the study area (Figure S4b; Amani et al. (2017)).

3.2. Methods

3.2.1. InSAR Processing

The InSAR Computing Environment (ISCE) software was used to produce over 970 and 280 Sentinel-1 and Envisat interferograms, respectively (see Figure 3). Temporal and perpendicular baseline thresholds were set to 1800 days and 1070 m for the Envisat data. For Sentinel-1 data, interferograms were formed between each epoch and the four preceding and four subsequent epochs. To reduce the speckle noise and increase processing speed, the interferograms were resampled to ~90 and ~30 m for the Envisat and Sentinel-1 datasets, respectively. The topographic phase was removed using the 1-arcsec Shuttle Radar Topography Mission (SRTM) Digital Elevation Model (DEM) (Jarvis et al., 2008). The statistical-Cost Network-Flow Algorithm for Phase Unwrapping (SNAPHU) was used for phase unwrapping (Chen & Zebker, 2003). As deformation rates before and after large data gaps in 2007 were consistent, a joint rate (linear fit + offset) was calculated for the descending Envisat dataset (Figure S5). A similar approach was also used to combine the individual
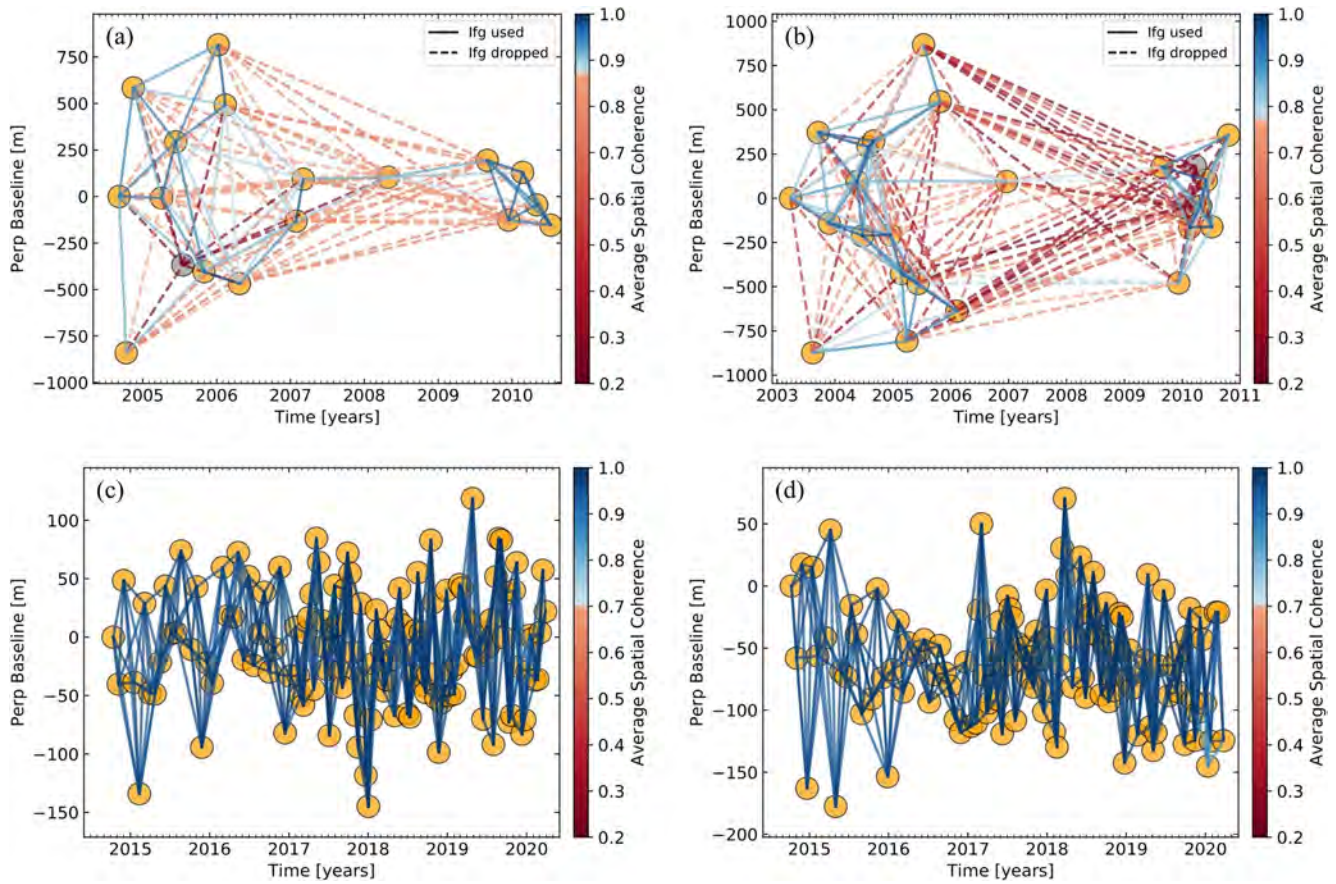
Figure 3. Envisat and Sentinel-1 interferograms visualized in the spatial and temporal baseline domains and color-coded by average spatial coherence. (a) Envisat ascending, (b) Envisat descending, (c) Sentinel-1 ascending, and (d) Sentinel-1 descending. Dashed lines in (a) and (b) illustrate Envisat interferograms dropped when applying the average spatial coherence thresholds. Solid lines show interferograms inverted to retrieve the time series of surface deformation.

Envisat time series into a single time series, assuming constant subsidence rates, as suggested by individual time series.

We use the Small BAseline Subset (SBAS) time series method (Berardino et al., 2002) implemented in the Miami INsar Time-series software in PYthon (MintPy) (Yunjun et al., 2019) to invert a network of interferograms and retrieve surface displacement through time. In MintPy, average spatial coherence thresholds of 0.87 and 0.77 (Figure 3) were used to remove outliers affected by unwrapping errors (Tizzani et al., 2007) for the Envisat ascending and descending, respectively. The tropospheric delay was corrected using PyAPS (Jolivet et al., 2011, 2014) and the ECMWF Reanalysis v5 (ERA-5) weather model with a spatial resolution of 31 km (Hersbach et al., 2020). Regional phase ramps caused by long-wavelength tropospheric and ionospheric delays and orbital errors were removed by a linear ramp calculated at each acquisition. The empirical model of Marinkovic and Larsen (2013) was used to correct the Local Oscillator Drift of the Envisat ASAR datasets and to improve the geo-location accuracy of the Envisat interferograms. Finally, the displacement time series were all referenced to a single pixel that exhibits high coherence (cross in Figure 5).

Ascending and descending time series were combined to calculate the vertical and east-west components, assuming no contributions from the north-south component (Wright et al., 2004), by minimizing as:

$$\begin{bmatrix} v_e \\ v_u \end{bmatrix} = U \cdot \begin{bmatrix} d_e \\ d_u \end{bmatrix} - R_{\text{LOS}} \tag{1}$$

where $d = \left(d_e, d_u\right)^T$ is the 2D deformation vector (east-west, vertical); (v_e, v_u) are the observation residuals, and $U = \begin{bmatrix} \sin\left(\theta_A\right).\cos\left(\varnothing_A\right) & \cos\left(\theta_A\right) \\ \sin\left(\theta_D\right).\cos\left(\varnothing_D\right) & \cos\left(\theta_D\right) \end{bmatrix}$ is a matrix, including the Line-Of-Sight (LOS) vectors, where θ is the incidence angle value for each Distributed Scatterer and $\varnothing$ is the satellite-heading angle for each orbit. R_{LOS} contains the LOS measurements for the ascending and descending orbits. If the covariance matrix for errors in the LOS measurements is $\sum_R$, by minimizing the observation residuals, the deformation vector $d = -\left(U^T.\sum_R^{-1}.U\right)^{-1}.U^T.\sum_R^{-1}.R$ can be calculated with a weighted least-squares inversion. The covariance matrix for the vector components is $\sum_d = \left(U^T.\sum_R^{-1}.U\right)^{-1}$ and, as errors in LOS measurements are independent in the ascending and descending measurements, we get

$$\sum_d = \sigma^2 \left(U^T.U\right)^{-1} \qquad (2)$$

where $\sigma^2 = \begin{bmatrix} \sigma_A^2 & 0 \\ 0 & \sigma_D^2 \end{bmatrix}$; and σ_A^2 and σ_D^2 are the standard deviations for the ascending and descending orbits, respectively. The square root of the diagonal terms of $\sum_d$ gives a standard displacement error that can be considered as uncertainties in space over the YAP. InSAR uncertainties in time were calculated by averaging a 31×31 pixels window near the reference point at each time step of the ascending and descending time series for both the Envisat and Sentinel-1 datasets.

3.2.2. GWL Changes and Ground Displacement

To assess the potential relationship between the GWL changes and the observed deformation, we gather time series of vertical displacement and of GWL at the locations of piezometers. To generate time series of vertical displacement from the LOS Sentinel-1 ascending and descending time series, we calculate the pixel-wise horizontal-to-vertical ratios from the mean horizontal and vertical velocity maps and multiplied the LOS deformation at each pixel by the corresponding ratio (assuming that the ratio of horizontal-to-vertical displacement at each pixel is constant throughout the Sentinel-1 observation period). During the period of record, converted-vertical displacements are computed in two-week intervals while the GWL changes are available monthly. Due to this temporal sampling difference, we compare duration curves of converted-vertical displacements to GWL changes.

A duration curve illustrates the data variability in the frequency domain by illuminating the proportion of the data that exceeds the given value of data. Duration curves are widely used to characterize streamflow variability over different time steps (e.g., daily, monthly, and yearly) (Castellarin et al., 2004; Ghotbi, Wang, Singh, Bloschl, et al., 2020, Ghotbi, Wang, Singh, Mayo, et al., 2020b; Vogel & Fennessey, 1994). The duration curves of GWL changes and vertical displacement (referred to hereafter as GDC for Groundwater Duration Curves and DDC for Displacement Duration Curves, respectively) are computed from the 2014–2018 data. For computing the GDC, monthly GWL changes are sorted in decreasing order and are each attributed a rank (e.g., rank $m = 1,2, ..., n$) with the rank n corresponding to the smallest GWL change. The probability of the ranked GWL change (i.e., GWL_i where $= 1, 2, ..., n$) is a probability that GWL is greater than the given ranked value (GWL_i), and is computed with the Weibull method i.e., $P_i = m/n + 1$ (Vogel & Fennessey, 1994). The GDC shows GWL_i as a function of P_i with the central part of duration curves (i.e., 30th to 70th percentiles) representing the long-term variability (Sawicz et al., 2011) while other parts of duration curves are related to the high and low variabilities of the GWL changes and vertical displacement. As such, to quantify the long-term variability from duration curves, we compute the corresponding slope S_{DC} (Yadav et al., 2007):

$$S_{DC} = \frac{Y_{30\%} - Y_{70\%}}{0.70 - 0.30} \qquad (3)$$

where $Y_{30\%}$ and $Y_{70\%}$ are the values (e.g., GWL_{30} and GWL_{70} or D_{30} and D_{70}), corresponding to the 30th and 70th percentiles of exceedance probability, respectively.
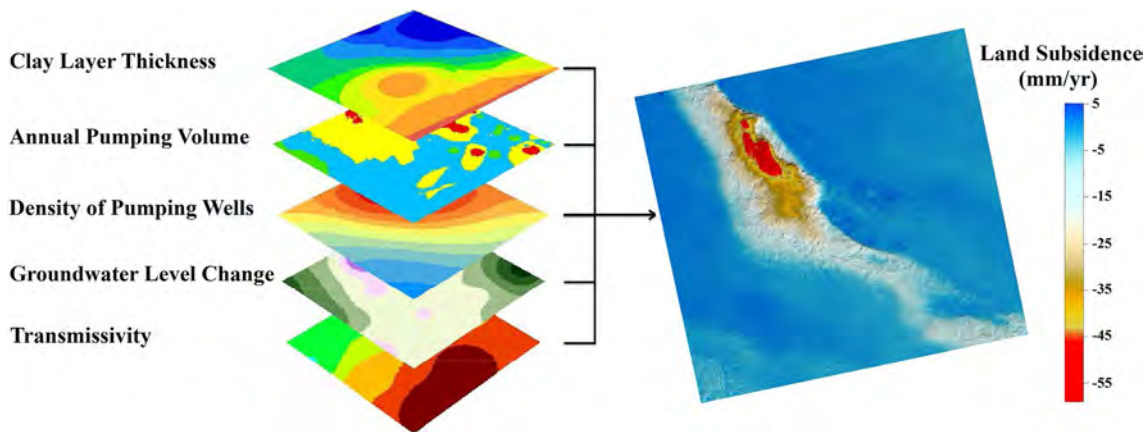
Figure 4. Schematic representation of the datasets used in the statistical methods to explore the controls on the subsidence rates and extent to the potential predictor variables (e.g., clay layer thickness, density of pumping wells, annual pumping volume, groundwater level change, and transmissivity (see Figure S2)).

3.2.3. Statistical Modeling Methods

To explore the controls on the land subsidence rates and extent, we compare the observed vertical deformation to vertical deformation simulated by potential predictor variables (clay layer thickness, density of pumping wells, GWL changes, annual pumping volume, and transmissivity; Figure 4; [SHIBASAKI, 1969]) through (a) a Multi-Linear Regression (MLR) approach and (b) a Support Vector Machine Regression (SVR) (Abdollahi et al., 2019; Tien Bui et al., 2018; Vapnik, 1995) approach. A MLR, with Y and X_i, representing the observed response (land subsidence) and the potential predictor variables, respectively, and a_0 a regression constant and a_i the coefficients of the model follows:

$$Y = a_0 + a_1 \times X_1 + a_2 \times X_2 + ... + a_i \times X_i \qquad (4)$$

We use the Statistics and Machine Learning Toolbox of MathWorks and a linear epsilon-insensitive SVR (ε-SVR) approach, also known as $L1$ loss (MathWorks, 2019). In ε-SVR, training data include the values of potential predictor variables and the observed response (Figure 4) with the goal of finding a function $f(x)$ which can be linear, quadratic, cubic, fine-gaussian, medium-gaussian, or coarse-gaussian (MathWorks, 2019) that deviates from the observed response values (y_n) by a value no greater than ε for a multivariate set of the potential predictor variables (x_n) (Chen et al., 2006).

3.2.4. Elastic Versus Inelastic Aquifer Response

Determining whether land subsidence is irrecoverable (inelastic) or recoverable (elastic) is important for water resources management strategies. Chaussard and Farr (2019) proposed a new method to separate elastic from inelastic behavior of deformation with an Independent Component Analysis (ICA), assuming that the independent sources have been linearly combined in the original signal (Gualandi et al., 2017). We apply the fixed-point algorithm, FastICA (Hyvärinen & Oja, 1997) and use a Principal Component Analysis (PCA) and the truncation of variance rule to impose the number of independent components (ICs) and their order of importance (Cattell, 1966; Chaussard et al., 2017). We reply on the Sentinel-1 data, which has 1,408,439 samples per epoch and 118 and 129 epochs (acquisitions between 2014 and 2020) for the descending and ascending orbits, respectively. Following the PCA results, only one component explains ~99.5% of the eigenvalues (compared to 99.6% with two components). We display an eigenvalue time series for each IC to represent its magnitude at each epoch, as well as, a score map, which has been scaled by the contribution of retained components to the original data and highlights the pixels with the observed eigenvalue time series.
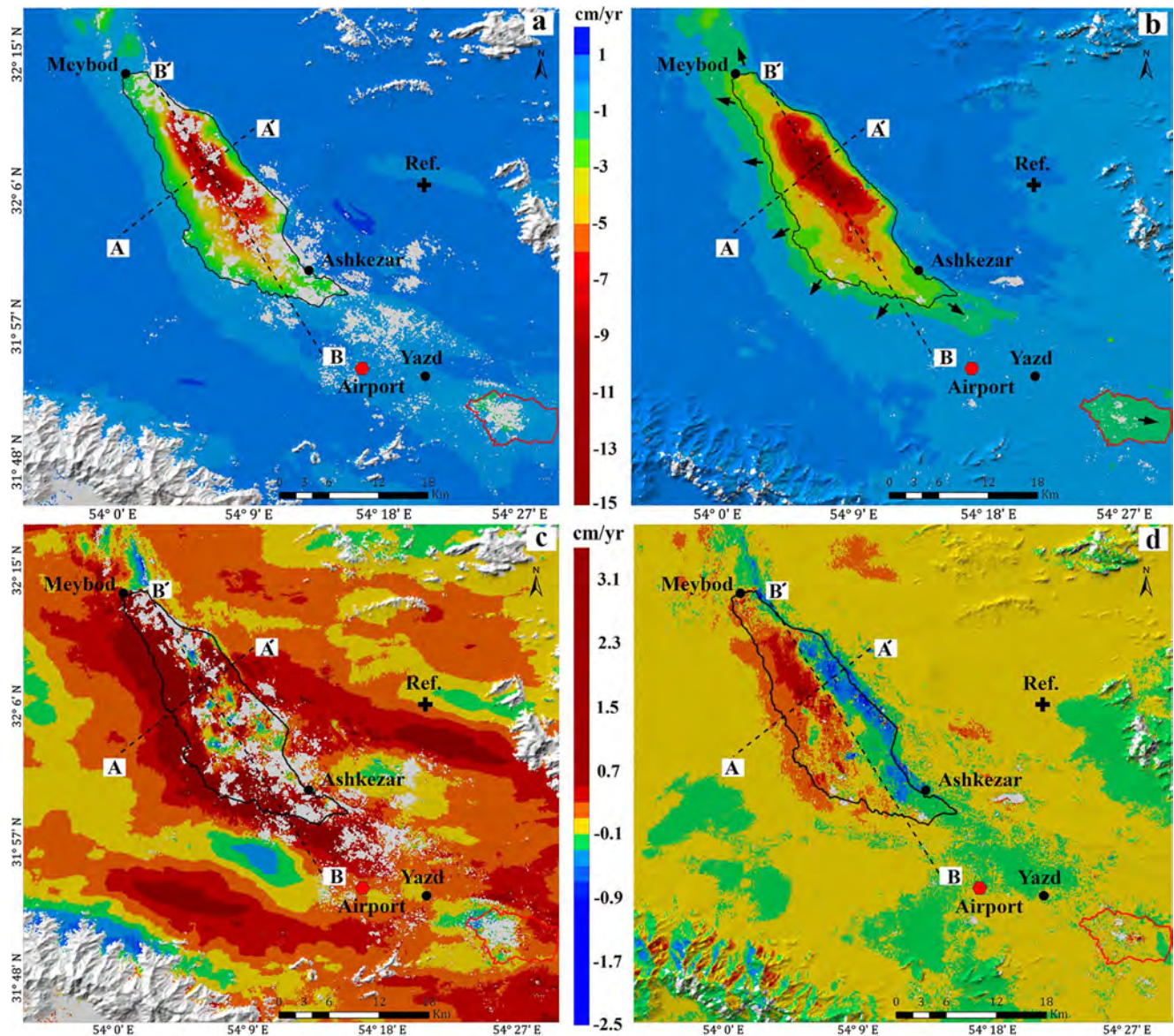
Figure 5. Annual mean deformation rate maps of the vertical component from (a) Envisat and (b) Sentinel-1 data, and the horizontal component from (c) Envisat and (d) Sentinel-1 data. Red colors show downward and eastward movements in the vertical and horizontal maps, respectively. Blue colors show westward movement in the horizontal component and areas of little or no deformation in the vertical maps. The black and red circles indicate cities and the Yazd Sadooghi International Airport (YSIA), respectively. The dashed lines show the locations of the two profiles $(A - A')$ and $(B - B')$ in Figure 7. The cross indicates the reference pixel located in a stable area. The black and red polygons indicate the Main Subsidence Feature and a new subsidence area to the southeast of Yazd city, respectively. The arrows in (b) indicate the direction of growth of the two subsiding areas.

4. Results and Analysis

4.1. Spatiotemporal Pattern of Subsidence

The spatiotemporal pattern of subsidence in the YAP is analyzed. Figure 5 shows the mean vertical and horizontal velocity maps in the YAP, decomposed by the mean LOS velocity from ascending and descending orbits (Figure S6). The most significant subsidence feature is an elongated northwest-southeast zone, south of Meybod and north of Ashkezar (dark circles in Figures 5a and 5b). This zone of subsidence, referred to as the Main Subsidence Feature (MSF), covers an area of 234.45 km² (Figure 5) and is seen in both Envisat and Sentinel-1 datasets. While the overall shape and boundary of the MSF are consistent over the 17 years of InSAR data, the displacement rates and spatial extents appear to have changed over time. The MSF extent
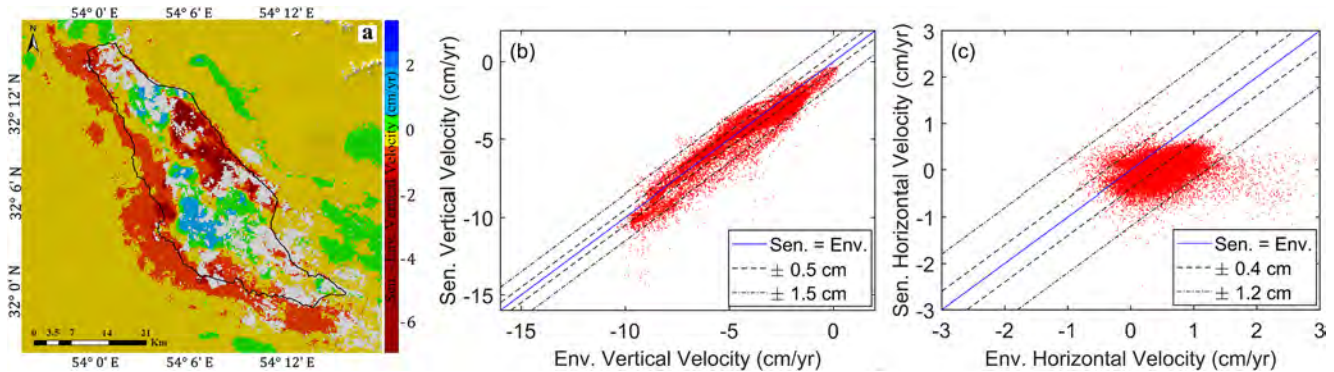
Figure 6. (a) Differential vertical velocity map between the Envisat and Sentinel data (Figures 5a and 5b). The black polygon shows the boundary of the Main Subsidence Feature (MSF). Comparison between Envisat and Sentinel-1 (b) vertical velocities and (c) horizontal velocities over the MSF. The differential vertical rates fall within a three-sigma range of ±1.5 cm/yr (dash-dotted lines), while the Sentinel-1 and Envisat horizontal motions do not appear correlated.

has grown westward and toward the Yazd and Meybod cities in the Sentinel data, with a subsidence rate of ~2 cm/yr in areas that appeared stable in the Envisat data (indicated with the arrows in Figure 5b). A differential vertical velocity map between the Envisat and Sentinel data (Figure 6a) confirms that the subsidence has expanded laterally along the southern and western boundaries of the MSF. In Figure 6a, both an increase and a decrease in the trend of subsidence by 2 cm/yr and 0.8 cm/yr are seen in the northeast and southwest parts of the MSF, respectively, while a new subsidence area is detected southeast of Yazd city (red polygon in Figure 5b). Figure 6b shows a good agreement between the Envisat and Sentinel vertical motions (with a correlation of 0.95 and a standard deviation of 0.7 cm/yr), while Figures 6c, 7c and 7d show that the Sentinel-1 and Envisat horizontal motions differ significantly, likely due to the greater uncertainties of the Envisat data (Figure 3). The 2014–2020 Sentinel-1 data reveals eastward ground motion of 1.5 cm/yr on the western side of the MSF and westward motion at 1.2 cm/yr on the eastern side of the MSF (Figure 5d). Although Figure S2b shows that the distribution of pumping wells is low in these areas with opposite horizontal motions, the volume of water extracted appears to be sufficient to create this inner zone of contraction (Helm, 1994).

The profiles in Figures 7a and 7b confirm that the Envisat and Sentinel-1 data detect significant differences e.g., the greater 2014–2020 (Sentinel-1) subsidence rates (a) on profile A-A' between 5 and 10 km (Figure 7a, shaded area), and (b) on profile B-B' between 0 and 7 km (Figure 7b, shaded area), highlighting the expansion of the subsiding area towards the south. In addition, both profiles show that in the center of the MSF subsidence rates accelerated by about 5 cm/yr between the Envisat and Sentinel-1 data. A localized area with almost 14 cm/yr of subsidence is observed for 20 pixels in the Sentinel-1 data (peak in Figure 7b) and may represent failing/sinking of an engineered highway overpass (Figure S7a). Figure S7 shows the coherence at these pixels in all interferograms from the Sentinel-1 ascending and descending datasets. It can be seen that the temporal coherence of all pixels is consistently greater than 0.5, confirming that unwrapping errors, which are the dominant source of the processing errors in local subsidence estimation and tends to occur in low coherence areas (Zhao et al., 2016), are unlikely. Figure 7c confirms the existence of eastward motion on the west side of the MSF and a westward motion on the east side in the Sentinel-1 data. Figure 7d shows no clear east-west deformation in the N-S oriented profile and further illustrates the greater noise of the Envisat data. The uncertainties of both vertical and horizontal rates along the profiles are shown in the inset plots with Sentinel-1 data having a standard deviation of about 1 mm/yr along both profiles and Envisat of 2–4 mm/yr (see Figure S8 for maps of uncertainties). Over the entire study area, uncertainties are mostly <2 mm/yr with means of 0.6 and 0.4 mm/yr for the Envisat and Sentinel-1 vertical components, and 0.4 and 0.3 mm/yr for the Envisat and Sentinel-1 horizontal components, respectively (Figure S8). Similarly, the majority of uncertainties for both the ascending and descending epochs of the Envisat and Sentinel-1 data are <2 mm (Figure S9).
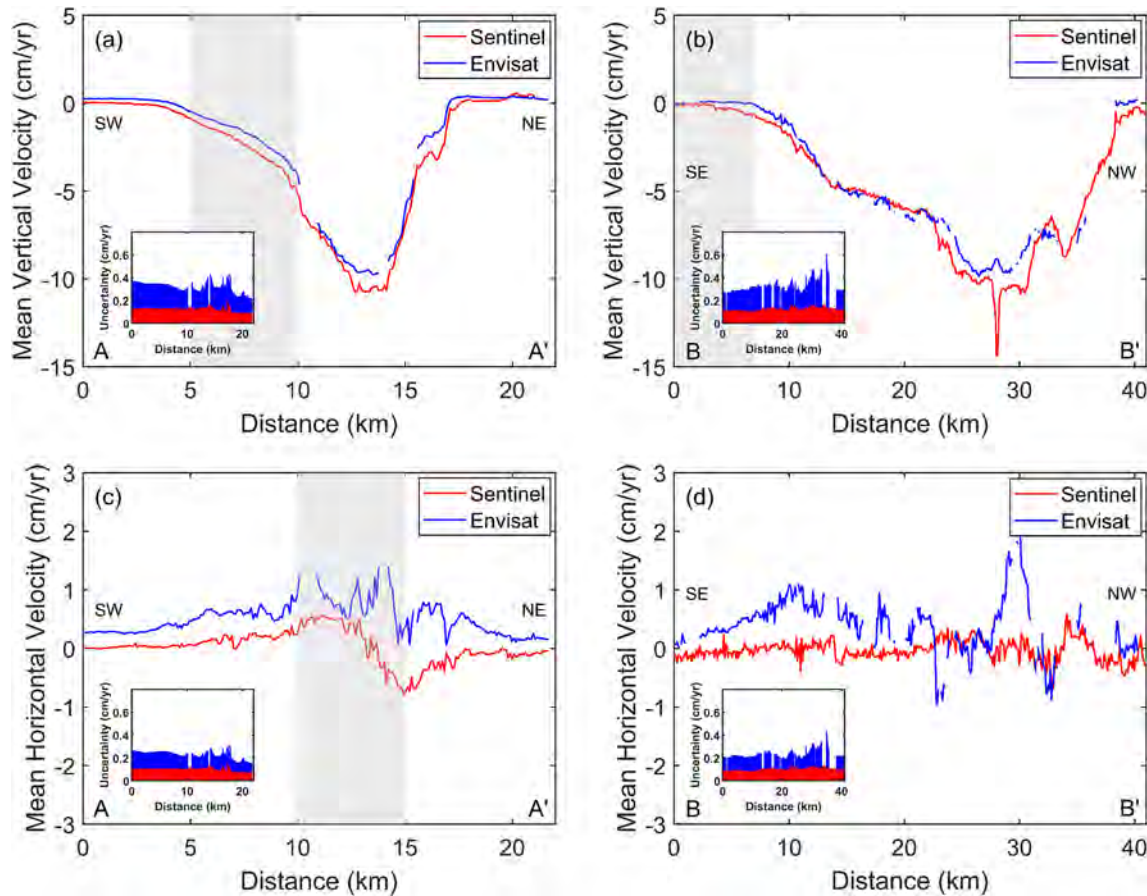
Figure 7. Mean vertical (a), (b) and horizontal (c), (d) velocities derived from Envisat (blue) and Sentinel-1 (red) data along the profiles $(A - A')$ and$(B - B')$ (locations shown in Figure 5). The insets show the corresponding three-sigma uncertainties. The shaded areas highlight significantly different signals in the 2003–2010 Envisat and 2014–2020 Sentinel-1 data mentioned in the text.

4.2. Infrastructure Monitoring

Comparison of our data with optical imagery reveals that land subsidence at varying rates occurs in agricultural lands, urban areas, and industrial areas, potentially affecting factories and infrastructures, such as roads and power grids. Table S5 provides a list of the infrastructures located in subsiding areas. One of the most important infrastructures in the YAP is the Bandar Abbas-Yazd-Ardakan Transit road. Figures 8b–8e highlights the mean vertical and horizontal velocities along different sections of the road as seen in the Sentinel-1 data. Section (A) experiences rapid subsidence over a 40 km section with a peak subsidence rate of 14 cm/yr, without significant horizontal motion. About 1.5 km south-southwest of this section and 2 km northeast of nearest residential areas (red circle in Figure 8a), differential subsidence led to multiple ground fissures (Figure 9). Section (B) experiences vertical displacement along a 25 km long section with a peak value of 13 cm/yr and no significant horizontal deformation. Section (C) experiences subsidence in the northernmost 10 km with a peak of 1.7 cm/yr and no significant horizontal motion.

Another important transportation structure is the 85-km-long Tehran-Bandar Abbas railway connecting the Yazd province to the Provinces of Isfahan and Kerman. This section, known as the Santo section, is one of the most trafficked rail lines of Iran. Figure 8e reveals two ~20 km-long subsiding sections with rates of 1.7 and 1.4 cm/yr, respectively, and no significant horizontal deformation. Subsidence of up to 2 cm/yr is also observed near the Yazd Sadooghi International Airport (YSIA) (see location in Figure 5), which served 431,500 passengers in 2012, making it the 11th airport in Iran (Iranian Students' News Agency, 2013).
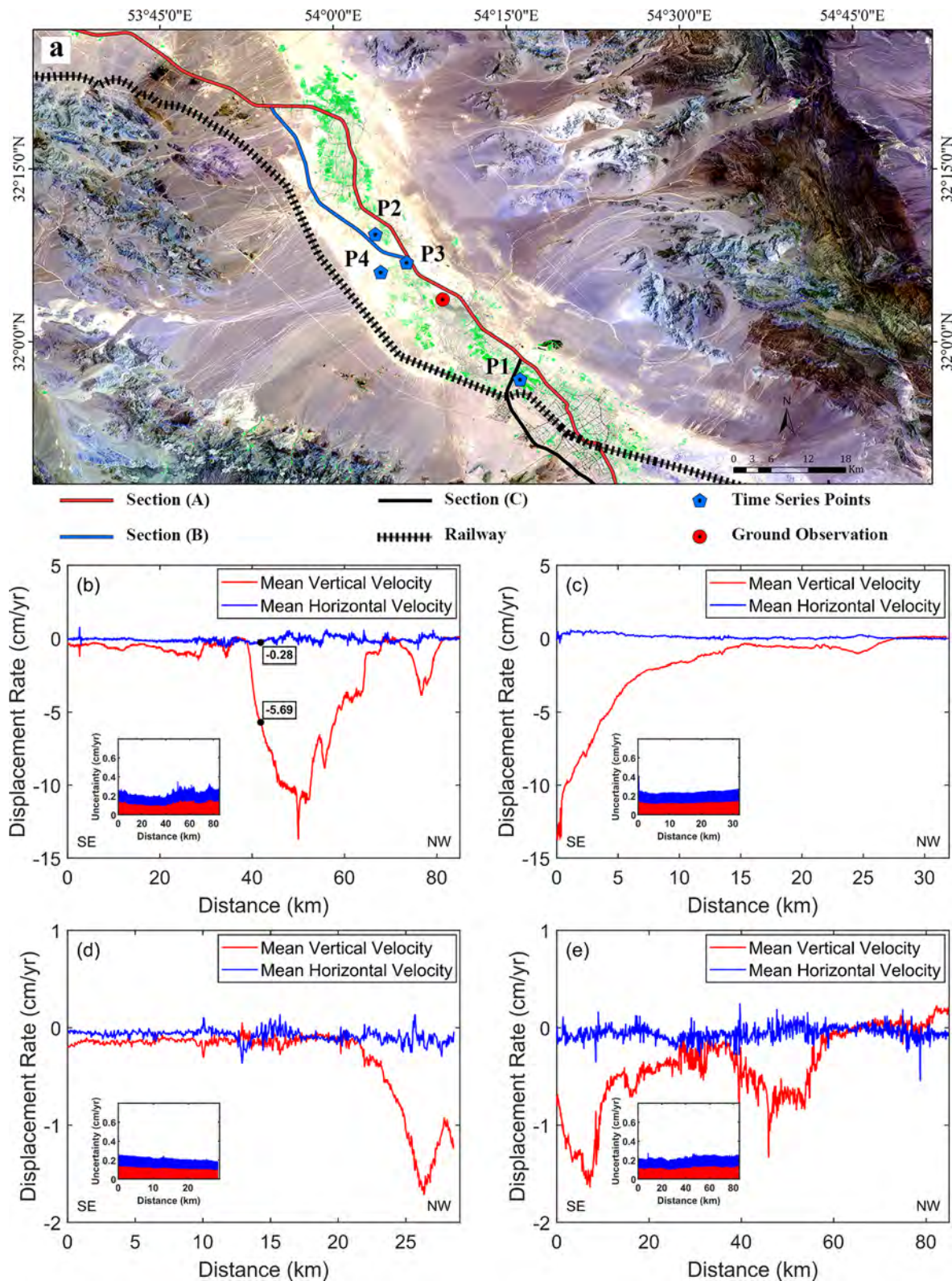
Figure 8.

Figure 9. Photograph looking South taken from the location of the red circle on Figure 8a which illustrates the fissures that have developed as a result of the observed differential subsidence (the person shows the scale).

4.3. Potential Causes of Land Subsidence

To gain further insights into the controls that hydrogeological and geological parameters may have on the rate and extent of the land subsidence, we carry out the following analysis using the vertical component of deformation while the rate and pattern of the horizontal component of deformation will be explored in further detail in future work.

4.3.1. Hydrogeological Conditions

Figure S3a–S3b shows that between 2004 and 2019, a 3.2°C increase (0.2°C/yr) in the average LST occurred in the region. Figure S3b shows that the LST was consistently higher throughout 2019 compared to 2004 (with the exception of January). Figure S3c shows that precipitation in 2018 amounted to approximately only half of the 2003 precipitation (Sharafi & Karim, 2020), and while annual precipitation is highly variable, there is an overall trend towards decreasing rainfall in recent decades. These climatic changes (increased temperature and decreased precipitation) have likely led to an increased degree of dryness (Figure S4b), which in turn influences natural recharge and discharge from evapotranspiration.

In addition, the Statistics Center of Iran reported a significant population growth of 3.67% per year between 1956 and 2016 (Fanni, 2006) in the cities located in the YAP (Figures 1b and S10), leading to increased agricultural and industrial activities (e.g., tile and steel) (see Figure 1c), which influences groundwater usage (Figure S1). GWL fluctuations in the aquifer over 44 years (1974–2018) (Figure 10) reveal an average 18 m drop in the YAP aquifer (Figure 10a). Figure 10b shows that 4,010 million cubic meters (MCM) were extracted from the aquifer during this period with 90%, 6.2%, and 3.8% used by the agriculture, urban, and industry sectors, respectively (Fig. S1b–S1e) (Iran's WRM Co., 2014).

To assess the potential relationship between the GWL changes and observed deformation, the time series of converted-vertical displacement (see Section 3.2.2) and GWL changes were determined at sites P1-P4 (locations shown in Figure 8a). The converted-vertical displacement time series from the ascending data do not differ significantly from vertical time series converted from the descending data (Figure S11). We use the ascending, converted-vertical displacement time series, which has 11 more acquisitions than the descending data, to compare to the GWL fluctuations in the probability and time domains (see method in Section 3.2.2, Figure S12).

Correlation values of 0.67 and 0.81 are observed between the converted-vertical displacements and the GWL changes at P1 and P4, respectively (Figure S11), suggesting that GWL changes may influence the subsidence

Figure 8. (a) Locations of the Bandar Abbas-Yazd-Ardakan Transit road sections (shown by the red, blue, and black lines), and of the railway (dashed black line). Blue and red symbols indicate the locations of time series (Figure S11) and ground observation sites (Figure 9), respectively. Mean Sentinel-1 vertical (red) and horizontal (blue) velocities for (b) Section (A), (c) Section (B), (d) Section (C) of the Badar Abbas-Yazd-Ardakan transit road, and (e) the Tehran-Bandar Abbas railway. The insets show the corresponding uncertainties. Black points in (a) indicate the mean Sentinel-1 vertical and horizontal velocities for the projected location of ground observation site on Section (A).
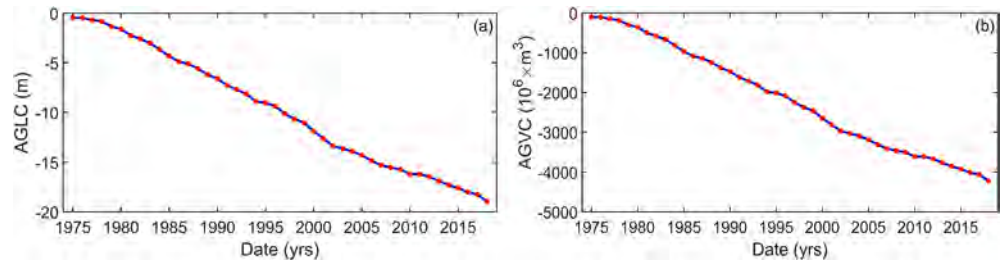
Figure 10. (a) Average annual accumulated groundwater level changes (AGLC) in meters (mean lowering of groundwater level of aquifer) and (b) total annual accumulated groundwater volume changes (AGVC) in the million cubic meters for the Yazd-Ardakan Plain aquifer system between 1974 and 2018 (Iran's WRM Co., 2014).

rates. At P2, although the time series of GWL changes and converted-vertical displacements have a correlation of 0.7, their trends differ significantly. Finally, at P3, the correlation between the converted-vertical displacements and the GWL changes is only 0.21 (Figure S11), suggesting that other factors also influence the subsidence rates.

Figure 11 shows the exceedance probability (EP) analysis of converted-vertical displacements and GWL changes. The duration curves of converted-vertical displacements (DDC) and GWL changes (GDC) mirror each other at P1 and P4, confirming that, at those locations, the GWL changes and subsidence rates are related. In contrast, at P2, the slopes S_{DC} of the GDC and DDC do not track one another, suggesting that other factors affect the subsidence rates. At P3, for EP < 0.2, the S_{DC} of the GWL changes is greater than that of the converted-vertical displacements, while for EP > 0.2, the S_{DC} for the GDC is smaller. These observations suggest that the subsidence rates at P2 and P3 cannot be predicted solely from the observed GWL changes. It is worth noting that P2 and P3 are located in the area with the thickest clay deposits (Figure S2a).

4.3.2. Geological Settings

We explore the potential influence of the shallow clay layer thickness on the subsidence rates and extent. The clays thickness increases towards the center of the basin, reaching 134 meters (Figure S2a). We separate the clay thickness (C) observed throughout the YAP into five classes (C ≤ 20 m, 20 m < C ≤ 40 m, 40 m < C ≤ 60 m, 60 m < C ≤ 80 m, and C > 80 m (Table 1)) and compare the observed maximum and mean vertical velocities observed in areas of the valley corresponding to each class (Table 1). The maximum
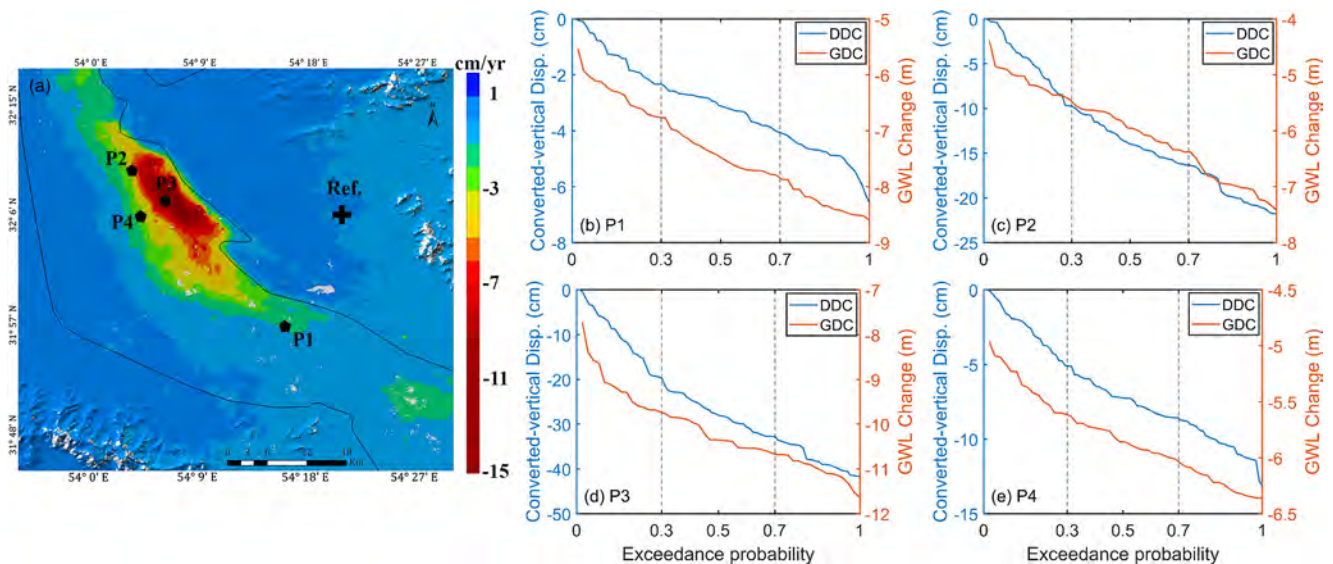
Figure 11. (a) Mean 2014–2020 Sentinel-1 vertical velocity map. The cross and black circles indicate the reference pixel and the P1-P4 site locations, respectively. (b–e) Duration curves of groundwater level changes (GDC, red) and converted-vertical displacements (DDC, blue) for P1 to P4 ((b) to (e), respectively).

Table 1
Maximum and Mean Vertical Velocities Observed in Areas With Various Clay Thicknesses

Clay layer thickness (C) (m)	Dataset	Statistical parameters (cm/yr)		
		Max	Mean	Std
C ≤ 20	Envisat	5.1	0.7	0.6
	Sentinel	5.7	0.9	0.7
20 < C ≤ 40	Envisat	5.6	0.6	0.9
	Sentinel	5.6	0.8	1.1
40 < C ≤ 60	Envisat	6.2	1.0	1.2
	Sentinel	6.1	1.3	1.4
60 < C ≤ 80	Envisat	7.2	0.8	1.2
	Sentinel	6.4	1.1	1.4
C > 80	Envisat	10.8	4.4	2.8
	Sentinel	14.6	4.9	2.8

vertical velocities (>10 cm/yr) observed in the Envisat and Sentinel-1 data are located in areas with clay thicknesses >80 m. In contrast, areas with clay thicknesses ≤20m show subsidence rates ≤6 cm/yr. These observations suggest that the clay thickness is an important factor influencing the subsidence rates and extent.

4.4. Relative Control on the Rates and Extent of Observed Land Subsidence

To quantify the relative importance of hydrological and geological parameters previously described (i.e., the clay layer thickness, annual pumping volume, GWL changes, density of pumping wells, and transmissivity) on the observed land subsidence rates and extent, we use MLR and SVR approaches (linear and non-linear regression methods, see method Section 3.2.3; Figure 12, and Table 2). Due to the low spatial resolution of climate parameters (LST and precipitation), we do not use those variables in the MLR and SVR approaches. To estimate the goodness of fit and compare the results with each other, we use the Relative RMSE (RRMSE = RMSE / average $\left(\text{mean vertical velocity}\right)$) and r-squared ($R^2$) values.

Figure 12 shows that the single-variable MLR and SVR approaches, with the clay layer thickness as a potential predictor, have the highest R^2 and lowest RRMSE of all single-variable analyses, suggesting that the clay layer thickness has the strongest influence on the land subsidence rates (RRMSEs of 0.95–1.32 and R^2 of 0.42–0.67). Among the bivariate analyses, incorporating the clay layer thickness and the density of pumping wells improves the R^2 by 26% and 34% for the Envisat data (MLR and SVR, respectively) and 15% and 25% for the Sentinel-1 data (MLR and SVR, respectively); and decrease the RRMSE by 10% and 30% for the Envisat data and 8% and 29% for the Sentinel-1 data (Table 2). These results suggest that the density of pumping wells is the second most influential parameter after the clay thickness. Figure 12 further confirms that the multi-variable analyses in which the clay layer thickness is considered as a potential predictor variable perform best.

In addition, Table 2 shows that the SVR method performs better than the MLR method, decreasing the RRMSE between the predicted and observed subsidence by 66% for the Envisat and 77% for the Sentinel-1 datasets and increasing the R^2 by 58% for the Envisat and 61% for the Sentinel-1 datasets over the MLR approach. The better performance of the SVR is likely due to its nonlinearity, which is more accurate but also difficult to interpret (MathWorks, 2020). Including all potential predictor parameters (instead of only the clay layer thickness) decreases the value of RRMSE by 66% for the Envisat and 76% for the Sentinel-1 datasets in the SVR and 17% for the Envisat and 15% for the Sentinel-1 datasets in the SVR. These results suggest that within the YAP, all parameters likely influence in various proportions the subsidence rates and extent, with the clay thickness being the dominant control.

We perform a sensitivity analysis to quantify the relative importance of each potential predictor variables to the predicted land subsidence using the MLR method (Li & Merchant, 2013; Parizi et al., 2019) as follow:

$$\text{PV}\left(j\right) = \frac{\text{AV}_{\text{rw}}\left(j\right) - \text{AV}_{\text{rw}}}{\text{AV}_{\text{rw}}} \times 100 \tag{5}$$

where *PV* is the percentage of variation in the predicted subsidence; $\text{AV}_{\text{rw}}\left(j\right)$ is the predicted annual subsidence (with j representing each potential predictor variable), and AV_{rw} is the predicted annual land subsidence considering all potential predictor variables. Figure 13 shows that the clay thickness is the dominant parameter in explaining the variability of land subsidence rates. The pumping well density is the second most influential parameter, and other parameters have a significantly lower relative importance. In other words, for a similar distribution of pumping wells and annual pumping volume, thicker clays experience greater compaction.
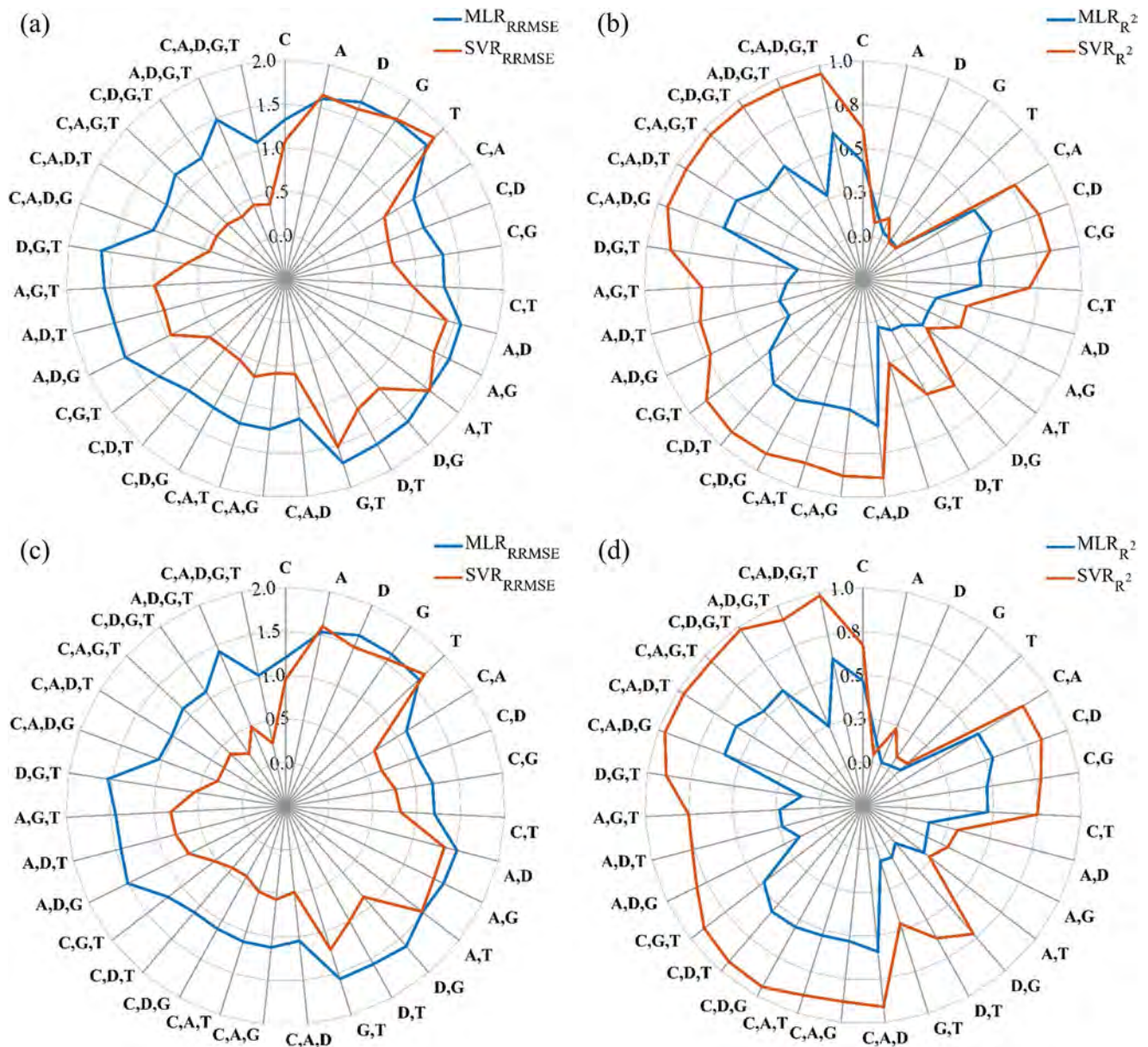
Figure 12. Spider plots illustrating the values of Relative RMSE (RRMSE) (a) and (c) and r-squared (R^2) (b) and (d) for all single- and multi-variable Multi-Linear Regression (MLR) and SVR analyses using several potential predictor variables (i.e., C: Clay Layer Thickness (m), A: Annual Pumping Volume (m³/yr), D: Density of Pumping Well (Number/km²), G: Groundwater Level (GWL) Change (m/yr), T: Transmissivity (m²/day) and the observed land subsidence from the Envisat (a),(b) and Sentinel-1 datasets (c), (d).

4.5. Elastic Versus Inelastic Behavior

When an aquifer system experiences greater groundwater-level lowering than previously experienced (i.e., the stress exceeds the pre-consolidation stress), pore spaces collapse permanently, resulting in inelastic deformation (Carlson et al., 2020), which may manifest itself in the formation of surface fissures and cracks in areas of large differential compaction. Because the inelastic compressibility of aquitards is one to three orders of magnitude larger than the elastic compressibility of aquitards and aquifers (Pavelko, 2004; Riley, 1998), most inelastic deformation occurs in aquitard layers (Chaussard, Burgmann et al., 2014, 2017).

While Figure S11 shows no resolvable seasonal variations in the time series of deformation for the four selected points (P1–P4), performing time series analysis of deformation at each pixel is necessary to ensure

Table 2
Results of a Multi-Linear Regression (MLR) Approach and a Support Vector Machine Regression (SVR) Approach Considering the Mean Vertical Velocity (MVV) as a Response Variable and the Other Variables as Potential Predictor Variables (Figure S2)

Variable(s)	Regression type	Dataset	Model type[a]/Kernel function	R^2	RRMSE
C	MLR	Envisat	$MVV = -0.026 \times C + 0.054$	0.42	1.32
	SVR		Fine Gaussian	0.61	1.08
	MLR	Sentinel-1	$MVV = -0.039 \times C - 0.015$	0.47	1.20
	SVR		Fine Gaussian	0.67	0.95
C D	MLR	Envisat	$MVV = -0.028 \times C - 0.820 \times D + 0.547$	0.53	1.18
	SVR		Fine Gaussian	0.82	0.75
	MLR	Sentinel-1	$MVV = -0.042 \times C - 1.032 \times D + 0.649$	0.54	1.11
	SVR		Fine Gaussian	0.84	0.67
C D A G K	MLR	Envisat	$MVV = -0.025 \times C - 0.860 \times D - 1.612E{-}6 \times A + 0.191 \times G + 0.0002 \times T + 0.693$	0.60	1.09
	SVR		Fine Gaussian	0.95	0.37
	MLR	Sentinel-1	$MVV = -0.039 \times C - 1.143 \times D - 2.076E{-}6 \times A + 0.489 \times G + 0.0004 \times T + 0.887$	0.61	1.02
	SVR		Fine Gaussian	0.98	0.23

Note. The r-squared (R^2) and Relative RMSE are used to estimate the goodness of fit. In the SVR, the kernel functions (i.e., Gaussian or Radial Basis Function (RBF), Linear, Quadratic, and Cubic) determine the applied nonlinear transformation to the data before the SVM is trained (MathWorks, 2020).
[a]MVV: Mean Vertical Velocity (cm/yr), C: Clay Layer Thickness (m), A: Annual Pumping Volume (m³/yr), D: Density of Pumping Well (Number/km²), G: Groundwater Level (GWL) Change (m/yr), T: Transmissivity (m²/day).

that this is a consistent behavior across the entire YAP aquifer. In addition, the long-term subsidence, which is orders-of-magnitude greater than the seasonal deformation, may mask shorter-term signals. To explore the time and space variability that may be embedded in the deformation data and hidden by the dominant signal without relying on a priori constraints, we apply the ICA approach of Chaussard and Farr (2019) to the Sentinel-1 converted-vertical deformation time series (Figure 14).

The eigenvalue of one component (IC1) corresponds to 99.5% of the sum of all the non-zero eigenvalues, while a second component (IC2) retains only 0.1% of the eigenvalues. The spatial extent of the IC1 positive score values is comparable to the mean vertical Sentinel-1 velocity map (Figure 5b), while the IC1 eigenvector time series highlights a nearly linear trend between 2014 and 2020 with a slope of −2.1 (in eigenvector/year units) (−15.7 in cm/yr units) (Figure 14a). While IC1 is the only statistically significant component, we
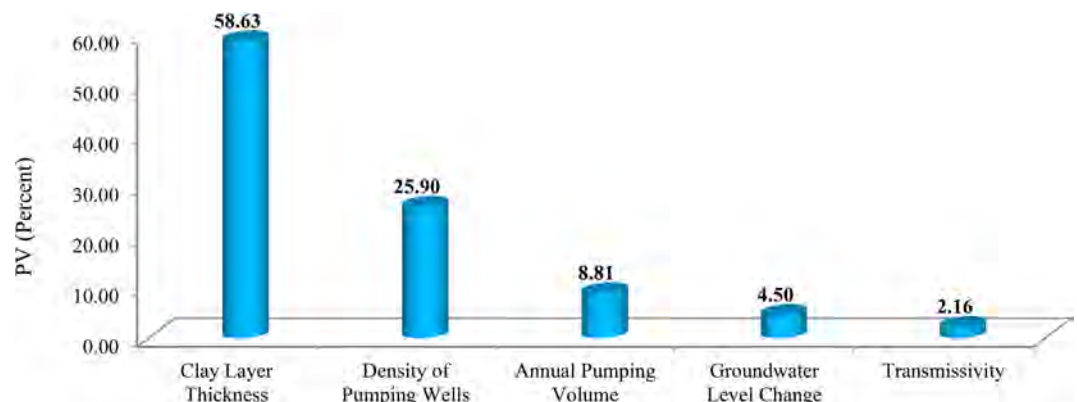
Figure 13. Percentage of variation (PV) of land subsidence explained by each of the potential predictor variables used in the MLR method.
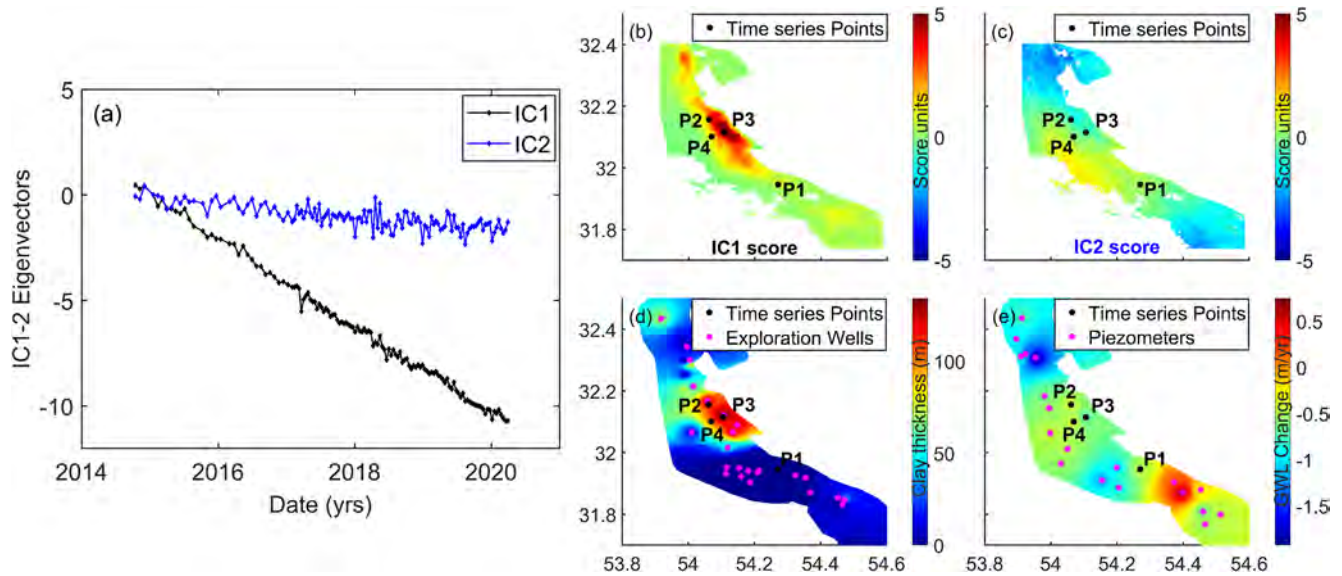
Figure 14. (a) Eigenvector time series analysis of IC1 (black) and IC2 (blue) derived from the converted-vertical-ascending Sentinel-1 data (see Figure S13 for corresponding results for the converted-vertical-descending orbit Sentinel-1 data). (b), (c) Score maps of (b) IC1 and (c) IC2. Black dots show the locations of the points with time series shown in Figure S11. (d) Map of the clay thickness interpolated between exploration wells (pink dots). (e) 2014–2020 mean GWL change map interpolated between piezometers (pink dots).

show the results of IC2 for reference. The IC2 score map shows negative values in the north and south and positive values in the west (Figure 14c), and an eigenvector time series with a slight downward trend and a slope of −0.3 (in eigenvector/year units) (−0.001 in cm/yr unit) (Figure 14a).

Figure 14d suggests a positive correlation between the spatial extent of positive IC1 score values (subsidence) and the clay layer thickness, while Figure 14e suggests a positive correlation between the extent of the northern area with positive score values in IC1 (subsidence) and the area with maximum GWL decline (blue in Figure 14e). Figure 14d also reveals that GWL declines ≥0.5 m/yr exist in the entirety of the area experiencing subsidence (positive score values in IC1). These observations suggest that the amplitude of the land subsidence is controlled by the thickness of the clay layer once a threshold of GWL decline is reached.

5. Discussion

To develop sustainable conservation plans for the aquifer system, it is important to know whether the observed deformation is dominantly recoverable (elastic) or irrecoverable (inelastic). The ICA results suggest that almost all the deformation observed in the YAP is inelastic and captured by the IC1. This is in agreement with observations made in the Mexico City (Chaussard et al., 2021) and contrasts with observations made in the Central Valley and the Santa Clara Valley aquifers, California, USA where multiple short-term elastic deformation signals were isolated (Chaussard & Farr, 2019; Chaussard, Wdowinski, et al., 2014, 2017). The long-wavelength spatial signal observed in the IC2, combined with the low slope observed in the eigenvector time series suggest that IC2 likely captures noise associated with orbital errors that are not entirely accounted for in the processing.

In addition, results from the MLR and SVR analyses suggest that the amplitude of the land subsidence is controlled by the thickness of the clay layer once a threshold of GWL decline is reached. These results confirm that (a) the deformation in the YAP is irreversible in locations where a minimum GWL is reached, leading to stress exceeding the pre-consolidation stress (which accounts for 85% of spatial extent of the subsiding area), and (b) in those locations, the subsidence rates are constant and mostly controlled by the clays-layer thickness. These results are similar to what was reported in Mexico City (Chaussard et al., 2021). These observations emphasize that to manage the YAP water resources, it is necessary to know the aquifer system characteristics and groundwater storage loss.

Following the literature (Castellazzi et al., 2018; Chaussard, Bürgmann, et al., 2014; Rezaei et al., 2020; Smith et al., 2017), we calculate the groundwater storage loss from our InSAR results. Based on the ICA results, we assume fully inelastic deformation and limit the analysis to the MSF where the aquifer is fully confined, and consider the periods of 2003–2011 and 2014–2018 (overlapping periods of piezometers and Envisat- and Sentinel-1 derived InSAR results). Table S6 shows that the storage loss values constrained by the piezometers and derived from InSAR deformation are comparable and reach 10.06 MCM per year between 2003 and 2011, and 10.99 MCM per year between 2014 and 2018. Compared to the annual groundwater storage loss in several aquifers in the world e.g., Central Valley in California (0.091 MCM per km^2; (Miller et al., 2020)), Madrid in Spain (0.018 MCM per km^2; (Béjar-Pizarro et al., 2017)), San Joaquin Valley in California (0.016 MCM per km^2; (Smith et al., 2017)), and Cangzhou in China (0.004 MCM per km^2; (Jiang et al., 2018)), the annual groundwater storage loss of 0.04 MCM per km^2 for the YAP aquifer is considerable and shows the need to develop a sustainability plan.

6. Conclusions

InSAR time series analysis of Envisat and Sentinel-1 data from 2003 to 2020 reveals land subsidence in the YAP at rates up to 15 cm/yr within an elongated northwest-southeast zone of approximately 234.45 km^2. While the overall shape of the subsiding area did not change over the past 17 years, it grew laterally. Our data also reveals eastward motion at ~1.5 cm/yr and westward motion at ~1.2 cm/yr on the western and eastern sides of the subsiding area, respectively, as a result of the radial strain changes across the subsiding zone. Over 25 km of the Bandar Abbas-Yazd-Ardakan Transit road is affected by subsidence rates up to 5 cm/yr and the nearby airport (YSIA) is subsiding at ~2 cm/yr. While the YAP experienced a significant lowering in the groundwater levels in the past decades, regression analyses and duration curves of GWL changes and displacements at sites P2 and P3 show that the thickness of a shallow clay layer has the greatest correlation with the observed subsidence rates. Finally, the Independent Component Analysis (ICA) reveals that almost all the subsidence observed in the YAP is inelastic and thus irreversible, which is caused by clay compaction. The clay layer aquitard is draining at constant rates, resulting in the observed, effectively linear subsidence rates. These results highlight the need to develop and enforce sustainable water management strategies to protect the infrastructure and groundwater resources in central Iran.

Data Availability Statement

The Envisat original data are copyrighted by the European Space Agency (ESA) and provided freely through the ESA archive (https://esar-ds.eo.esa.int/oads/access/). The Sentinel-1 data are made available by the ESA and distributed and archived through the Alaska Satellite Facility (ASF) (https://www.asf.alaska.edu/sentinel/). The hydrological and geological data (i.e., groundwater level, logs of exploration wells, pumping wells, and precipitation) are found through contacting the Regional Water Company of Yazd (https://www.yzrw.ir/?l=EN) and the Geological Survey and Mineral Explorations of Iran (GSI) (https://gsi.ir/en) respectively. The InSAR time series deformation and average deformation rate products, and population density and weather data can be accessed online with the following link in a public repository (https://doi.org/10.5281/zenodo.5138189). LST data are obtained from the Google Earth Engine Data Catalog (https://developers.google.com/earth-engine/datasets). The ERA5 data and Shuttle Radar Topography Mission (SRTM) DEM data are provided through the Copernicus Climate Data Store (https://cds.climate.copernicus.eu/#!/home) and the NASA's Land Processes Distributed Active Archive Center (LP DAAC), located at the USGS Earth Resources Observation and Science (EROS) Center (https://e4ftl01.cr.usgs.gov/MEASURES/), respectively. The Miami INsar Time-series software in PYthon (MintPy), InSAR Computing Environment (ISCE) software, and Python 3 Atmospheric Phase Screen (PyAPS) are the open-source and available on (https://github.com/insarlab/MintPy), (http://earthdef.caltech.edu/#), and (https://github.com/isce-framework/isce2), respectively.

References

Abdollahi, S., Pourghasemi, H. R., Ghanbarian, G. A., & Safaeian, R. (2019). Prioritization of effective factors in the occurrence of land subsidence and its susceptibility mapping using an SVM model and their different kernel functions. *Bulletin of Engineering Geology and the Environment*, *78*, 4017–4034. https://doi.org/10.1007/s10064-018-1403-6

Abidin, H. Z., Djaja, R., Darmawan, D., Hadi, S., Akbar, A., Rajiyowiryono, H., et al. (2001). Land subsidence of Jakarta (Indonesia) and its geodetic monitoring system. *Natural Hazards*, *23*, 365–387. https://doi.org/10.1023/a:1011144602064

Amani, M., Salehi, B., Mahdavi, S., Masjedi, A., & Dehnavi, S. (2017). Temperature-vegetation-soil moisture dryness index (TVMDI). *Remote Sensing of Environment*, *197*, 1–14. https://doi.org/10.1016/j.rse.2017.05.026

Amelung, F., Galloway, D. L., Bell, J. W., Zebker, H. A., & Laczniak, R. J. (1999). Sensing the ups and downs of Las Vegas: InSAR reveals structural control of land subsidence and aquifer-system deformation. *Geology*, *27*, 483–486. https://doi.org/10.1130/0091-7613(1999)027<0483:stuado>2.3.co;2

Amighpey, M., & Arabi, S. (2016). Studying land subsidence in Yazd province, Iran, by integration of InSAR and levelling measurements. *Remote Sensing Applications: Society and Environment*, *4*, 1–8. https://doi.org/10.1016/j.rsase.2016.04.001

Amin, A., & Bankher, K. (1997). Causes of land subsidence in the Kingdom of Saudi Arabia. *Natural Hazards*, *16*, 57–63. https://doi.org/10.1023/a:1007942021332

Anderssohn, J., Wetzel, H.-U., Walter, T. R., Motagh, M., Djamour, Y., & Kaufmann, H. (2008). Land subsidence pattern controlled by old alpine basement faults in the Kashmar Valley, northeast Iran: Results from InSAR and levelling. *Geophysical Journal International*, *174*, 287–294. https://doi.org/10.1111/j.1365-246x.2008.03805.x

Avtar, R., Tripathi, S., Aggarwal, A. K., & Kumar, P. (2019). Population–Urbanization–Energy Nexus: A Review. *Resources*, *8*, 136. https://doi.org/10.3390/resources8030136

Babaee, S., Mousavi, Z., Masoumi, Z., Malekshah, A. H., Roostaei, M., & Aflaki, M. (2020). Land subsidence from interferometric SAR and groundwater patterns in the Qazvin plain, Iran. *International Journal of Remote Sensing*, *41*, 4780–4798. https://doi.org/10.1080/01431161.2020.1724345

Baum, R. L., Galloway, D. L., & Harp, E. L. (2008). *Landslide and land subsidence hazards to pipelines*. Geological Survey (US). https://doi.org/10.3133/ofr20081164

Béjar-Pizarro, M., Ezquerro, P., Herrera, G., Tomás, R., Guardiola-Albert, C., Hernández, J. M. R., et al. (2017). Mapping groundwater level and aquifer storage variations from InSAR measurements in the Madrid aquifer, Central Spain. *Journal of Hydrology*, *547*, 678–689. https://doi.org/10.1016/j.jhydrol.2017.02.011

Bell, J. W., Amelung, F., Ferretti, A., Bianchi, M., & Novali, F. (2008). Permanent scatterer InSAR reveals seasonal and long-term aquifer-system response to groundwater pumping and artificial recharge. *Water Resources Research*, *44*, W02407. https://doi.org/10.1029/2007wr006152

Berardino, P., Fornaro, G., Lanari, R., & Sansosti, E. (2002). A new algorithm for surface deformation monitoring based on small baseline differential SAR interferograms. *IEEE Transactions on Geoscience and Remote Sensing*, *40*, 2375–2383. https://doi.org/10.1109/tgrs.2002.803792

Bozzano, F., Esposito, C., Franchi, S., Mazzanti, P., Perissin, D., Rocca, A., & Romano, E. (2015). Understanding the subsidence process of a quaternary plain by combining geological and hydrogeological modelling with satellite InSAR data: The Acque Albule Plain case study. *Remote Sensing of Environment*, *168*, 219–238. https://doi.org/10.1016/j.rse.2015.07.010

Bürgmann, R., Rosen, P. A., & Fielding, E. J. (2000). Synthetic aperture radar interferometry to measure Earth's surface topography and its deformation. *Annual Review of Earth and Planetary Sciences*, *28*, 169–209. https://doi.org/10.1146/annurev.earth.28.1.169

Carlson, G., Shirzaei, M., Ojha, C., & Werth, S. (2020). Subsidence-derived volumetric strain models for mapping extensional fissures and constraining rock mechanical properties in the San Joaquin Valley, California. *Journal of Geophysical Research: Solid Earth*, *125*, e2020JB019980. https://doi.org/10.1029/2020jb019980

Castellarin, A., Galeati, G., Brandimarte, L., Montanari, A., & Brath, A. (2004). Regional flow-duration curves: Reliability for ungauged basins. *Advances in Water Resources*, *27*, 953–965. https://doi.org/10.1016/j.advwatres.2004.08.005

Castellazzi, P., Longuevergne, L., Martel, R., Rivera, A., Brouard, C., & Chaussard, E. (2018). Quantitative mapping of groundwater depletion at the water management scale using a combined GRACE/InSAR approach. *Remote Sensing of Environment*, *205*, 408–418. https://doi.org/10.1016/j.rse.2017.11.025

Cattell, R. B. (1966). The Scree test for the number of factors. *Multivariate Behavioral Research*, *1*, 245–276. https://doi.org/10.1207/s15327906mbr0102_10

Chaussard, E., Amelung, F., Abidin, H., & Hong, S.-H. (2013). Sinking cities in Indonesia: ALOS PALSAR detects rapid subsidence due to groundwater and gas extraction. *Remote Sensing of Environment*, *128*, 150–161. https://doi.org/10.1016/j.rse.2012.10.015

Chaussard, E., Bürgmann, R., Shirzaei, M., Fielding, E. J., & Baker, B. (2014). Predictability of hydraulic head changes and characterization of aquifer-system and fault properties from InSAR-derived ground deformation. *Journal of Geophysical Research: Solid Earth*, *119*, 6572–6590. https://doi.org/10.1002/2014jb011266

Chaussard, E., & Farr, T. G. (2019). A new method for isolating elastic from inelastic deformation in aquifer systems: Application to the San Joaquin Valley, CA. *Geophysical Research Letters*, *46*, 10800–10809. https://doi.org/10.1029/2019gl084418

Chaussard, E., Havazli, E., Fattahi, H., Cabral-Cano, E., & Solano-Rojas, D. (2021). Over a century of sinking in Mexico City: No hope for significant elevation and storage capacity recovery. *Journal of Geophysical Research: Solid Earth*, *126*, e2020JB020648. https://doi.org/10.1029/2020jb020648

Chaussard, E., Milillo, P., Bürgmann, R., Perissin, D., Fielding, E. J., & Baker, B. (2017). Remote sensing of ground deformation for monitoring groundwater management practices: Application to the Santa Clara Valley during the 2012–2015 California drought. *Journal of Geophysical Research: Solid Earth*, *122*, 8566–8582. https://doi.org/10.1002/2017jb014676

Chaussard, E., Wdowinski, S., Cabral-Cano, E., & Amelung, F. (2014). Land subsidence in central Mexico detected by ALOS InSAR time-series. *Remote Sensing of Environment*, *140*, 94–106. https://doi.org/10.1016/j.rse.2013.08.038

Chen, C., & Zebker, A. (2003). *SNAPHU: Statisticalcost, network-flow algorithm for phase unwrapping*.

Chen, P.-H., Fan, R.-E., & Lin, C.-J. (2006). A study on SMO-type decomposition methods for support vector machines. *IEEE Transactions on Neural Networks*, *17*, 893–908. https://doi.org/10.1109/tnn.2006.875973

Cheremisinoff, N. P. (1998). *Groundwater remediation and treatment technologies*. Elsevier.

Conway, B. D. (2016). Land subsidence and earth fissures in south-central and southern Arizona, USA. *Hydrogeology Journal*, *24*, 649–655. https://doi.org/10.1007/s10040-015-1329-z

Emil, M. K., Sultan, M., Al-Akhras, K., Gebremichael, E., Izadi, M., & Karki, S. (2018). *Detecting and Monitoring Ground Deformation Using InSAR Time Series in Arid Environments; Doha City and its Surroundings* (Vol. *G41B-0704*): AGUFM.

Esfanjary, E. (2018). *Persian historic urban landscapes: Interpreting and managing Maibud over 6000 years*. Edinburgh University Press.

ESRI. (2012). Retrieved from http://desktop.arcgis.com/en/arcmap/latest/tools/spatial-analyst-toolbox/an-overview-of-the-interpolation-tools.htm

Fanni, Z. (2006). Cities and urbanization in Iran after the Islamic revolution. *Cities*, *23*, 407–411. https://doi.org/10.1016/j.cities.2006.08.003

Galloway, D. L., & Burbey, T. J. (2011). Regional land subsidence accompanying groundwater extraction. *Hydrogeology Journal*, *19*, 1459–1486. https://doi.org/10.1007/s10040-011-0775-5

Galloway, D. L., Hudnut, K. W., Ingebritsen, S., Phillips, S. P., Peltzer, G., Rogez, F., & Rosen, P. (1998). Detection of aquifer system compaction and land subsidence using interferometric synthetic aperture radar, Antelope Valley, Mojave Desert, California. *Water Resources Research*, *34*, 2573–2585. https://doi.org/10.1029/98wr01285

Geological Survey of Iran. (1997). Retrieved from https://gsi.ir/en

Ghotbi, S., Wang, D., Singh, A., Blöschl, G., & Sivapalan, M. (2020). A new framework for exploring process controls of flow duration curves. *Water Resources Research*, *56*, e2019WR026083. https://doi.org/10.1029/2019wr026083

Ghotbi, S., Wang, D., Singh, A., Mayo, T., & Sivapalan, M. (2020). Climate and Landscape controls of regional patterns of flow duration curves across the continental United States: Statistical approach. *Water Resources Research*, *56*, e2020WR028041. https://doi.org/10.1029/2020wr028041

Gido, N. A., Amin, H., Bagherbandi, M., & Nilfouroushan, F. (2020). Satellite monitoring of mass changes and ground subsidence in Sudan's oil fields using GRACE and Sentinel-1 data. *Remote Sensing*, *12*, 1792.

Gong, G., Mattevada, S., & O'bryant, S. E. (2014). Comparison of the accuracy of kriging and IDW interpolations in estimating groundwater arsenic concentrations in Texas. *Environmental Research*, *130*, 59–69. https://doi.org/10.1016/j.envres.2013.12.005

Gualandi, A., Avouac, J.-P., Galetzka, J., Genrich, J. F., Blewitt, G., Adhikari, L. B., et al. (2017). Pre-and post-seismic deformation related to the 2015, Mw7. 8 Gorkha earthquake, Nepal. *Tectonophysics*, *714*, 90–106. https://doi.org/10.1016/j.tecto.2016.06.014

Haghighi, M. H., & Motagh, M. (2019). Ground surface response to continuous compaction of aquifer system in Tehran, Iran: Results from a long-term multi-sensor InSAR analysis. *Remote Sensing of Environment*, *221*, 534–550. https://doi.org/10.1016/j.rse.2018.11.003

Hanson, R., Anderson, S., & Pool, D. (1990). *Simulation of ground-water flow and potential land subsidence, Avra Valley, Arizona*. US Department of the Interior, US Geological Survey.

Helm, D. C. (1994). Horizontal aquifer movement in a Theis-Thiem confined system. *Water Resources Research*, *30*, 953–964. https://doi.org/10.1029/94wr00030

Hersbach, H., Bell, B., Berrisford, P., Hirahara, S., Horányi, A., Muñoz-Sabater, J., et al. (2020). The ERA5 global reanalysis. *Quarterly Journal of the Royal Meteorological Society*, *146*, 1999–2049. https://doi.org/10.1002/qj.3803

Hoffmann, J., Zebker, H. A., Galloway, D. L., & Amelung, F. (2001). Seasonal subsidence and rebound in Las Vegas Valley, Nevada, observed by synthetic aperture radar interferometry. *Water Resources Research*, *37*, 1551–1566. https://doi.org/10.1029/2000wr900404

Hooper, A. (2008). A multi-temporal InSAR method incorporating both persistent scatterer and small baseline approaches. *Geophysical Research Letters*, *35*, L16302. https://doi.org/10.1029/2008gl034654

Hu, X., Lu, Z., & Wang, T. (2018). Characterization of hydrogeological properties in salt lake valley, Utah, using InSAR. *Journal of Geophysical Research: Earth Surface*, *123*, 1257–1271. https://doi.org/10.1029/2017jf004497

Hyvärinen, A., & Oja, E. (1997). A fast fixed-point algorithm for independent component analysis. *Neural Computation*, *9*, 1483–1492. https://doi.org/10.1162/neco.1997.9.7.1483

Iran Meteorological Organization. (2018). Retrieved from http://www.irimo.ir/eng/index.php

Iranian Students' News Agency. (2013). Retrieved from https://www.isna.ir/news/91101207946/

Iran's WRM Co. (2014). Retrieved from http://wrbs.wrm.ir/

Jarvis, A., Reuter, H., Nelson, A., & Guevara, E. (2008). *Hole-filled seamless SRTM data V4: International Centre for tropical agriculture (CIAT)*. Retrieved from http://srtm.csi.cgiar.org/

Jiang, L., Bai, L., Zhao, Y., Cao, G., Wang, H., & Sun, Q. (2018). Combining InSAR and hydraulic head measurements to estimate aquifer parameters and storage variations of confined aquifer system in Cangzhou, North China Plain. *Water Resources Research*, *54*, 8234–8252. https://doi.org/10.1029/2017wr022126

Jin, S., & Su, K. (2020). PPP models and performances from single-to quad-frequency BDS observations. *Satellite Navigation*, *1*, 1–13. https://doi.org/10.1186/s43020-020-00014-y

Jin, S. G., & Park, P. P. (2006). Strain accumulation in South Korea inferred from GPS measurements. *Earth Planets and Space*, *58*(5), 529–534. https://doi.org/10.1186/BF03351950

Jolivet, R., Agram, P. S., Lin, N. Y., Simons, M., Doin, M. P., Peltzer, G., & Li, Z. (2014). Improving InSAR geodesy using global atmospheric models. *Journal of Geophysical Research: Solid Earth*, *119*, 2324–2341. https://doi.org/10.1002/2013jb010588

Jolivet, R., Grandin, R., Lasserre, C., Doin, M. P., & Peltzer, G. (2011). Systematic InSAR tropospheric phase delay corrections from global meteorological reanalysis data. *Geophysical Research Letters*, *38*, L17311. https://doi.org/10.1029/2011gl048757

Julio-Miranda, P., Ortíz-Rodríguez, A., Palacio-Aponte, A., López-Doncel, R., & Barboza-Gudiño, R. (2012). Damage assessment associated with land subsidence in the San Luis Potosi-Soledad de Graciano Sanchez metropolitan area, Mexico, elements for risk management. *Natural Hazards*, *64*, 751–765. https://doi.org/10.1007/s11069-012-0269-3

Laity, J. J. (2009). *Deserts and desert environments*. John Wiley & Sons.

Li, R., & Merchant, J. W. (2013). Modeling vulnerability of groundwater to pollution under future scenarios of climate change and biofuels-related land use change: A case study in North Dakota, USA. *The Science of the Total Environment*, *447*, 32–45. https://doi.org/10.1016/j.scitotenv.2013.01.011

Marinkovic, P., & Larsen, Y. (2013). *Consequences of long-term ASAR local oscillator frequency decay—an empirical study of 10 years of data*.

MathWorks. (2019). Retrieved from https://www.mathworks.com/help/stats/understanding-support-vector-machine-regression.html

MathWorks. (2020). Retrieved from https://www.mathworks.com/help/stats/choose-regression-model-options.html

Miller, M. M., Jones, C. E., Sangha, S. S., & Bekaert, D. P. (2020). Rapid drought-induced land subsidence and its impact on the California aqueduct. *Remote Sensing of Environment*, *251*, 112063. https://doi.org/10.1016/j.rse.2020.112063

Motagh, M., Shamshiri, R., Haghighi, M. H., Wetzel, H.-U., Akbari, B., Nahavandchi, H., et al. (2017). Quantifying groundwater exploitation induced subsidence in the Rafsanjan plain, southeastern Iran, using InSAR time-series and in situ measurements. *Engineering Geology*, *218*, 134–151. https://doi.org/10.1016/j.enggeo.2017.01.011

Motagh, M., Walter, T. R., Sharifi, M. A., Fielding, E., Schenk, A., Anderssohn, J., & Zschau, J. (2008). Land subsidence in Iran caused by widespread water reservoir overexploitation. *Geophysical Research Letters*, *35*, L16403. https://doi.org/10.1029/2008gl033814

Ojha, C., Shirzaei, M., Werth, S., Argus, D. F., & Farr, T. G. (2018). Sustained groundwater loss in California's Central Valley exacerbated by intense drought periods. *Water Resources Research*, *54*, 4449–4460. https://doi.org/10.1029/2017wr022250

Parizi, E., Hosseini, S. M., Ataie-Ashtiani, B., & Simmons, C. T. (2019). Representative Pumping wells network to estimate groundwater withdrawal from aquifers: Lessons from a developing country, Iran. *Journal of Hydrology*, *578*, 124090. https://doi.org/10.1016/j.jhydrol.2019.124090

Pavelko, M. T. (2004). *Estimates of hydraulic properties from a one-dimensional numerical model of vertical aquifer-system deformation*. US Department of the Interior, US Geological Survey.

Porter, J. R., Xie, L., Challinor, A. J., Cochrane, K., Howden, S. M., Iqbal, M. M., et al. (2014). *Climate change 2014: Impacts, adaptation, and vulnerability. Part A: global and sectoral aspects. Contribution of Working Group II to the Fifth Assessment Report of the Intergovernmental Panel on Climate Change, Food security and food production systems, 2014*. (pp. 485–533).

Regional Water Company of Yazd. (2014). *Yazd water data. Internal reports*. Regional Water Company of Yazd.

Rezaei, A., Mousavi, Z., Khorrami, F., & Nankali, H. (2020). Inelastic and elastic storage properties and daily hydraulic head estimates from continuous global positioning system (GPS) measurements in northern Iran. *Hydrogeology Journal*, *28*, 657–672. https://doi.org/10.1007/s10040-019-02092-y

Riley, F. S. (1998). *Mechanics of aquifer systems—The scientific legacy of Joseph F. Poland* (pp. 13–27).

Sawicz, K., Wagener, T., Sivapalan, M., Troch, P. A., & Carrillo, G. (2011). Catchment classification: Empirical analysis of hydrologic similarity based on catchment function in the eastern USA. *Hydrology and Earth System Sciences*, *15*, 2895–2911. https://doi.org/10.5194/hess-15-2895-2011

Schmidt, D. A., & Bürgmann, R. (2003). Time-dependent land uplift and subsidence in the Santa Clara valley, California, from a large interferometric synthetic aperture radar data set. *Journal of Geophysical Research: Solid Earth*, *108*, 2895. https://doi.org/10.1029/2002jb002267

Sharafi, S., & Karim, N. M. (2020). Investigating trend changes of annual mean temperature and precipitation in Iran. *Arabian Journal of Geosciences*, *13*, 1–11. https://doi.org/10.1007/s12517-020-05695-y

Shibasaki, T. (1969). The hydrologic balance in the land subsidence phenomena. *Land Subsidence*, *1*, 201–215.

Smith, R. G., Knight, R., Chen, J., Reeves, J., Zebker, H., Farr, T., & Liu, Z. (2017). Estimating the permanent loss of groundwater storage in the southern San Joaquin V alley, California. *Water Resources Research*, *53*, 2133–2148. https://doi.org/10.1002/2016wr019861

Sterrett, R. J. (2007). *Groundwater and wells*. Johnson Screens.

TAMAB. (2004). *National groundwater resources status, basic studies office*. Iran Water Resources Management Company.

Tenzer, R., Chen, W., & Jin, S. G. (2015). Effect of the upper mantle density structure on the Moho geometry. *Pure and Applied Geophysics*, *172*(6), 1563–1583. https://doi.org/10.1007/s00024-014-0960-2

Tien Bui, D., Shahabi, H., Shirzadi, A., Chapi, K., Pradhan, B., Chen, W., et al. (2018). Land subsidence susceptibility mapping in south korea using machine learning algorithms. *Sensors*, *18*, 2464. https://doi.org/10.3390/s18082464

Tizzani, P., Berardino, P., Casu, F., Euillades, P., Manzo, M., Ricciardi, G., et al. (2007). Surface deformation of Long Valley caldera and Mono Basin, California, investigated with the SBAS-InSAR approach. *Remote Sensing of Environment*, *108*, 277–289. https://doi.org/10.1016/j.rse.2006.11.015

Trabelsi, N., Triki, I., Hentati, I., & Zairi, M. (2016). Aquifer vulnerability and seawater intrusion risk using GALDIT, GQI SWI and GIS: Case of a coastal aquifer in Tunisia. *Environmental Earth Sciences*, *75*, 669. https://doi.org/10.1007/s12665-016-5459-y

Vapnik, V. (1995). *The Nature of Statistical Learning Theory 6* (Vol. *1*, p. 995). Springer-Verlag.

Vogel, R. M., & Fennessey, N. M. (1994). Flow-duration curves. I: New interpretation and confidence intervals. *Journal of Water Resources Planning and Management*, *120*, 485–504. https://doi.org/10.1061/(asce)0733-9496(1994)120:4(485)

Walker, R., Gans, P., Allen, M., Jackson, J., Khatib, M., Marsh, N., & Zarrinkoub, M. (2009). Late Cenozoic volcanism and rates of active faulting in eastern Iran. *Geophysical Journal International*, *177*, 783–805. https://doi.org/10.1111/j.1365-246x.2008.04024.x

Walker, R., & Jackson, J. (2004). Active tectonics and late Cenozoic strain distribution in central and eastern Iran. *Tectonics*, *23*. https://doi.org/10.1029/2003tc001529

World Bank. (2005). *Islamic Republic of Iran: Cost assessment of environmental degradation*. Rural Development, Water and Environment Department32043-IR.

Wright, T. J., Parsons, B. E., & Lu, Z. (2004). Toward mapping surface deformation in three dimensions using InSAR. *Geophysical Research Letters*, *31*, L01607. https://doi.org/10.1029/2003gl018827

Yadav, M., Wagener, T., & Gupta, H. (2007). Regionalization of constraints on expected watershed response behavior for improved predictions in ungauged basins. *Advances in Water Resources*, *30*, 1756–1774. https://doi.org/10.1016/j.advwatres.2007.01.005

Yunjun, Z., Fattahi, H., & Amelung, F. (2019). Small baseline InSAR time series analysis: Unwrapping error correction and noise reduction. *Computers & Geosciences*, *133*, 104331. https://doi.org/10.1016/j.cageo.2019.104331

Zhao, C., Zhang, Q., He, Y., Peng, J., Yang, C., & Kang, Y. (2016). Small-scale loess landslide monitoring with small baseline subsets interferometric synthetic aperture radar technique—Case study of Xingyuan landslide, Shaanxi, China. *Journal of Applied Remote Sensing*, *10*, 026030. https://doi.org/10.1117/1.jrs.10.026030